▌ Inorganic Chemistry

Ag Nanoparticles/AgX (X=Cl, Br and I) Composites with Enhanced Photocatalytic Activity and Low Toxicological Effects

Marcelo Assis,[a] Francisco C. Groppo Filho,[a] Dayene S. Pimentel,[a] Thaiane Robeldo,[b] Amanda F. Gouveia,[a] Tassia F. D. Castro,[b] Hirla C. S. Fukushima,[b] Camila C. de Foggi,[a] João P. C. da Costa,[a] Ricardo C. Borra,[b] Juan Andrés,*[c] and Elson Longo[a]

Periodic structures induced by electron irradiation are a unique phenomenon when electron beams irradiate on the surface of some materials. These periodic structures have potential for technological applications. However, the fuzzy nature of the electron-induced structuring hinders its further exploration in such applications. In this paper, novel Ag nanoparticle/AgX (X=Cl, Br and I) composites, with enhanced photocatalytic activity and low toxicological effects, were prepared, for the first time, using electron beam irradiation. The remarkable advantage of this approach is that the Ag nanoparticles/AgX composites can be easily prepared in one-step without the need for high-pressure conditions, surfactants, ionic liquids, or reducing agents. Furthermore, our method does not involve any toxic substances, which makes the as-synthesized samples highly applicable for technological applications. The structure,

morphology and physicochemical properties of the Ag nanoparticles/AgX composites were studied using various characterization techniques. Using first-principles calculations based on density functional theory and the quantum theory of atoms in molecules, we reveal how the concentration of excess electrons in the AgX materials induces the formation of the Ag nanoparticles under electron beam irradiation. These results extend the fundamental understanding of the atomic process underlying the mechanism of Ag—X bond rupture observed during the transformation induced via electron irradiation of the AgX crystals by increasing the total number of electrons in the bulk structure. Thus, our findings provide viable guidance for the realization of new materials for the degradation of contaminated wastewater with low toxicity.

1. Introduction

Over the past decade, semiconductor photocatalyst has played a pivotal role in the fields of solar energy harvesting, clean chemical synthesis, photocatalytic antibacterial agents, and environmental technology due to its advantages over conventional heat-driven catalysis, which generally depend on high thermal energy that results in low product selectivity.[1–7] Among the semiconductors reported to date, silver halides, AgX; (X=Cl, Br and I) are a family of materials, which display a wide range of applications as antimicrobial agents,[8,9] catalysts for water oxidation,[10,11] and photocatalysts for environmental remediation.[12–15]

When a metal nanoparticle is excited at its localized surface plasmon resonance (SPR), the generated plasmon waves can enhance the local field, and then, an increase not only the absorption processes but also the efficiency of light-semiconductor interaction, at the semiconductor placed close to the metal nanoparticle, take place. This effect is employed in both individual materials for device applications and a lot of research is going on to understand these mechanisms.[16–18] Noble metal nanoparticles with SPR behavior have attracted a considerable amount of attention in the development of science and technology.[19] When they are immobilized on semiconductor surfaces have gained importance because they exhibit increased stability and high surface areas, which enhance the local field energy under visible light excitation through the SPR effect to promote the dual capability of adsorption and photocatalysis[19] when compared with their corresponding single-component materials. In particular, Ag nanoparticles is a good choice for surface modification because the price of Ag is much lower than those of Au, or even Pt, and Pd, and have exceptional optical, electronic, catalytic, and antibacterial properties.[20–27] Active materials decorated with Ag nanoparticles have shown superior performance in terms of their increased conductivity, catalytic activity, and sensing properties.[28–30] In particular, Ag nanoparticles deposited on the surface of wide band gap photocatalysts form metal/semiconductor materials and act as sensitizers to extend the light

[a] M. Assis, F. C. Groppo Filho, D. S. Pimentel, Dr. A. F. Gouveia, Dr. C. C. de Foggi, J. P. C. da Costa, Prof. E. Longo
CDMF, Universidade Federal de São Carlos, P.O. Box 676, 13565–905, São Carlos, São Paulo, Brazil

[b] T. Robeldo, T. F. D. Castro, Dr. H. C. S. Fukushima, Prof. R. C. Borra
LIA, Laboratory of Applied Immunology, Department of Genetics and Evolution, Universidade Federal de São Carlos, P.O. Box 676, 13565–905, São Carlos, São Paulo, Brazil

[c] Prof. J. Andrés
Department of Analytical and Physical Chemistry, University Jaume I (UJI), Castelló 12071, Spain
E-mail: andres@qfa.uji.es

Supporting information for this article is available on the WWW under https://doi.org/10.1002/slct.202000502

ChemistrySelect

Full Papers
doi.org/10.1002/slct.202000502

Chemistry Europe
European Chemical
Societies Publishing

absorption region and enhance efficient charge separation, i.e. a Schottky barrier is formed at the interface of the two materials and electrons flow from one material to the other (from the higher to the lower Fermi level) to align the Fermi energy levels.[31–36]

Recent reports have shown that highly efficient plasmonic photocatalysts such as Ag/g-C$_3$N$_4$, Ag/TiO$_2$, Ag/AgVO$_3$, Ag/Ag$_3$PO$_4$, Ag/Ag$_2$MoO$_4$, and Ag/Ag$_2$WO$_4$ can be prepared[13,37–43] and their results indicate that Ag decoration can dramatically enhance the photocatalytic performance of the pure photocatalyst via the SPR effect. Recently, considerable efforts have been placed on the design and fabrication of heterojunctions to improve the applications of AgX-based materials.[44–47] From the seminal work of Wang et al.,[48] in which a Ag/AgCl junction was formed, several methods have been carried out to improve the photocatalytic efficiency and stability of AgX using Ag nanoparticles.[49] Different Ag/AgX, X=Cl, Br and I based photocatalysts such as Ag/AgCl[50–54] and Ag/AgBr[55–57] have been prepared due to their excellent photocatalytic performance.

Many growth techniques and methods have been applied toward the fabrication of Ag/AgX heterostructures. Ag nanoparticles decorated on the surface of semiconductors are mainly prepared using different methods depending on the source of Ag nanoparticle used and include: i) The colloid route, ii) the reduction of metal salts,[38,58,59] iii) template-directed protocols using a surfactant or *in situ* self-assembly method,[60–63] iv) chemical reduction,[60] v) ultrasonic spray pyrolysis methods,[64] and vi) thermal-or light-induced[61] reduction of AgX and to generate metallic Ag particles on the surface of the AgX substrate. Very recently, Mao et al.[64] have employed an ultrasonic spray pyrolysis method to obtain Ag/AgX (X=Cl and Br) heterostructures. However, complex processes and harsh conditions are usually required using the methods mentioned beforehand.

Electron beam irradiation in the transmission electron microscopy (TEM) can be used to produce and manipulate nanostructures.[65–67] Our research group has presented an *in situ* method used to obtain Ag nanoparticles on the surface of a semiconductor, providing first-principles calculations in conjunction with experiments and advanced characterization to gain a deep insight into the formation of Ag nanoparticles and the nature of the mechanisms provoked by electron beam irradiation.[68–74] The formation process for Ag particles on AgCl crystals induced by electron beam irradiation has been previously reported,[67] while Formo et al. have analyzed AgCl: Ag and AgCl mesocubes with edge lengths of up to 500 nm.[75] Shi et al. have demonstrated that the growth of Ag nanoparticles is mainly related to the current density of the electron beam used.[76]

It is still a great challenge to obtain of Ag nanoparticle/AgX plasmonic photocatalysts via one-pot synthesis method. Making a breakthrough, it is essential to develop new techniques to produce metallic Ag nanoparticles on AgX materials in order to find new and innovative photocatalysis and ecofriendly agents. Due to its great relevance to human genetics, zebrafish is a vertebrate model of great interest in the study of toxicology and was used in this study.[77] The main focus of the present work is three-fold: (i) to demonstrate that the synthesis of Ag nanoparticles/AgX (X=Cl, Br and I) composites, by electron beam irradiation, opens up the door to obtain, *via* a facile and one-pot synthesis novel, materials with enhanced photocatalytic and toxicological activity, (ii) to find a relationship among the photocatalytic and toxicological activity, and the structure, morphology and physicochemical properties of the Ag nanoparticles/AgX composites, and (iii) to propose a mechanism to explain and elucidate the photocatalytic activity and toxicity.

2. Results and discussion

2.1. X-ray diffraction analysis

The long-range structural order was investigated using X-ray diffraction (XRD) for all the samples studied. Figure 1 shows the XRD patterns of the samples synthesized via a co-precipitation (CP) method in water for AgCl, AgBr and AgI before and after electron beam irradiation. All the XRD patterns display well-defined peaks, indicating a high degree of crystallization and long-range structural order.

For AgCl, no long-range changes were observed to occur upon electron irradiation (Figure 1A). The samples have a cubic structure ($a = 5.463$ Å), belonging to the space group $Fm\bar{3}m$ with four molecules per unit cell (Z=4), which was in accordance with the identification card in the *Inorganic Crystal Structure Database* (ICSD) (N° 56538).[90] Similar behavior was observed for the AgBr samples (Figure 1B). It was observed that electron beam irradiation does not change the long-range behavior of the materials, which have a cubic structure ($a = 5.772$ Å) and belongs to the space group $Fm\bar{3}m$ with four molecules per unit cell (Z=4). This was in accordance with the identification card in the ICSD (N° 56546).[90] The cubic phase of both AgCl and AgBr were formed by octahedral [AgX$_6$] clusters with coordination to six X=Cl and Br atoms, respectively.

In the case of the AgI samples (Figure 1C), hexagonal (β-AgI) and cubic (γ-AgI) phases were observed, since β-AgI is only obtained in its pure form via compression of tetragonal or rhombohedral structured AgI.[91] Both β-AgI and γ-AgI are made up of tetrahedral clusters with coordination to four I atoms [AgI$_4$]. The hexagonal phase ($a = 4.592$ Å and $c = 7.510$) belongs to the space group $P6_3mc$, with two molecules per unit cell (Z=2), which was in accordance with the identification card in the ICSD (N° 15589).[92] The cubic phase ($a = 6.499$ Å) belongs to the space group $F\bar{4}3m$ with four molecules per unit cell (Z= 4), which was in accordance with the identification card in the ICSD (N° 56552).[90]

After electron beam irradiation, a decrease in the amount of the γ-AgI cubic phase and the disappearance of the [400] peak of the cubic phase was observed, while a higher intensity of the [1$\bar{1}$0], [1$\bar{1}$1], [01$\bar{2}$] and [10$\bar{3}$] peaks of the hexagonal phase (β) was also observed. This occurs because the electron beam can transfer energy to a given material, causing atomic displacements, the introduction of vacancies, defect formation, crystallization etc. to occur until stabilized phases are obtained under these conditions due to a different arrangement of the
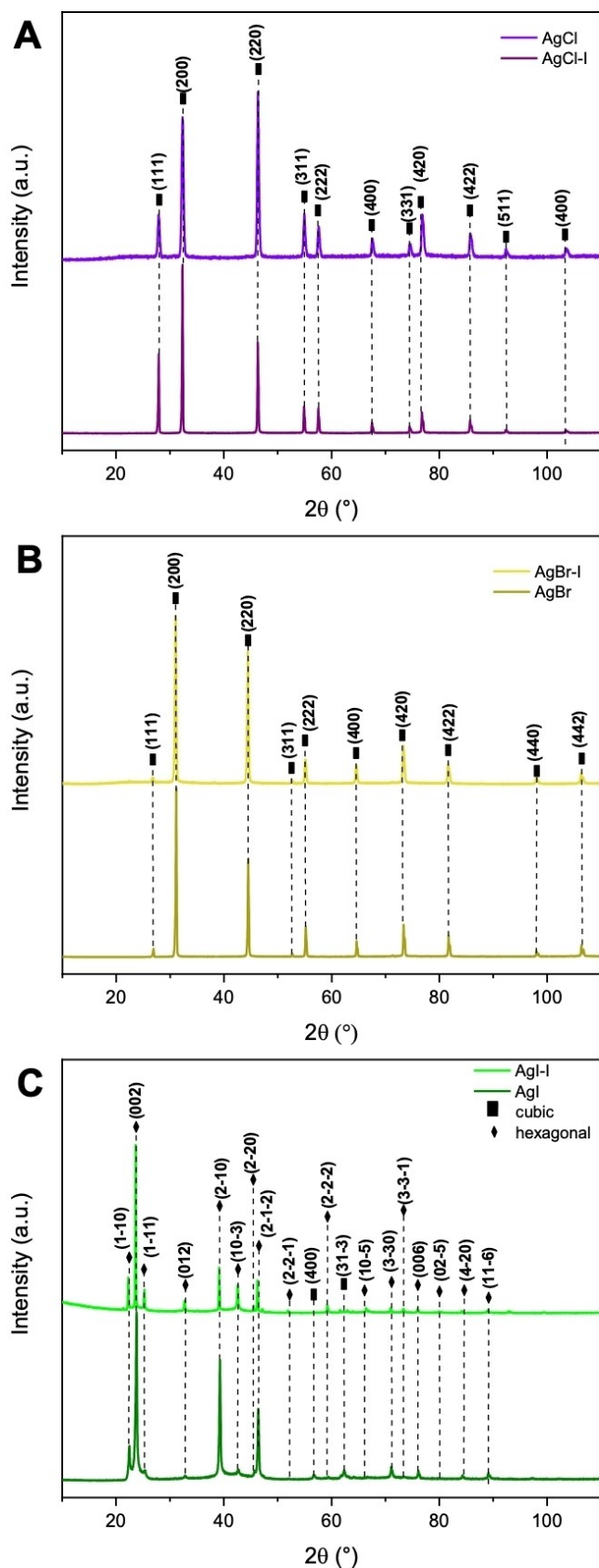
ChemistrySelect

Full Papers
doi.org/10.1002/slct.202000502

Chemistry Europe
European Chemical
Societies Publishing

Figure 1. XRD patterns for the samples of (A) AgCl, (B) AgBr and (C) AgI before and after irradiation with electron beam. Index I refers to the irradiated material.

atoms in the sample.[68,93–96] In this case, the stabilization of the hexagonal phase with respect to the cubic polymorph was observed.[97] It should also be noted that besides its high symmetry, the cubic phase is more compact than the hexagonal phase. The XRD results show that only a small region is irradiated by the electron beam, which causes the spontaneous displacement of the silver atoms, but does not destroying the long-range symmetry of the crystals.

2.2. Micro-Raman spectroscopy

Micro-Raman (MR) spectroscopy was performed as a complementary technique to XRD in order to evaluate the short-range structural order/disorder in the samples. Figure 2 shows the MR spectra recorded for all the samples studied. It was observed that electron beam irradiation caused small deviations in the structure to occur over a short distance. In the AgCl structure, the Cl anions can be connected in two different ways, as bridging atoms linking two metallic atoms or as terminal atoms.[98] For AgCl (Figure 2A), three Raman modes located at 60, 147 and 263 cm^{-1} were observed. The modes located at lower wavelengths (60 and 147 cm^{-1}) are related to the Ag lattice vibrational modes.[98,99] The mode located at 263 cm^{-1} is related to the stretching of the Ag−Cl bonds located at the terminal positions.[98,99] Because it belongs to the same point group, the MR spectrum recorded for the AgBr samples is very similar to AgCl. Three modes were observed at 63, 131, and 175 cm^{-1} for AgBr (Figure 2B). As-observed in AgCl, the low wavelength modes (63 and 131 cm^{-1}) are related to the Ag lattice vibrational modes, and the mode at 175 cm^{-1} was related to the stretching of the Ag–Br bonds.[99]

Two Raman modes were observed at 83 and 103 cm^{-1} for the AgI samples (Figure 2C). These modes are associated with the β-AgI polymorph and related to its E_2 and A_1 transitions, respectively.[91,100]

2.3. Optical properties: Ultraviolet-Visible and photoluminescence spectroscopy

The band gap energy (E_{gap}) was calculated using the method proposed by Kubelka-Munk and Wood-Tauc.[101,102] This principle is based on the transformation of diffuse reflection measurements and was used to estimate the E_{gap} values with good accuracy within the limits of the premises when modeled in three-dimensions. The presence of the 4d levels of the Ag+ cations in the valence band (VB) causes a strong hybridization with the p levels of the halides (Cl and Br), resulting in an indirect gap transition with E_{gap} values of 3.25 and 2.6 eV obtained for AgCl and AgBr, respectively.[103] Differently from AgCl and AgBr, both AgI (β and γ) phases have a direct gap transition with E_{gap} values of 2.91 and 3.69 eV obtained for β-AgI and γ-AgI, respectively.[104] This happens because unlike AgBr and AgCl, AgI has a rock salt structure with a center of inversion of symmetry.[104]

The E_{gap} values obtained for the samples are shown in Figure SI-1 (see Supporting Information). It was observed that the E_{gap} values obtained for the samples without electron beam

ChemistrySelect

Full Papers
doi.org/10.1002/slct.202000502

Chemistry Europe
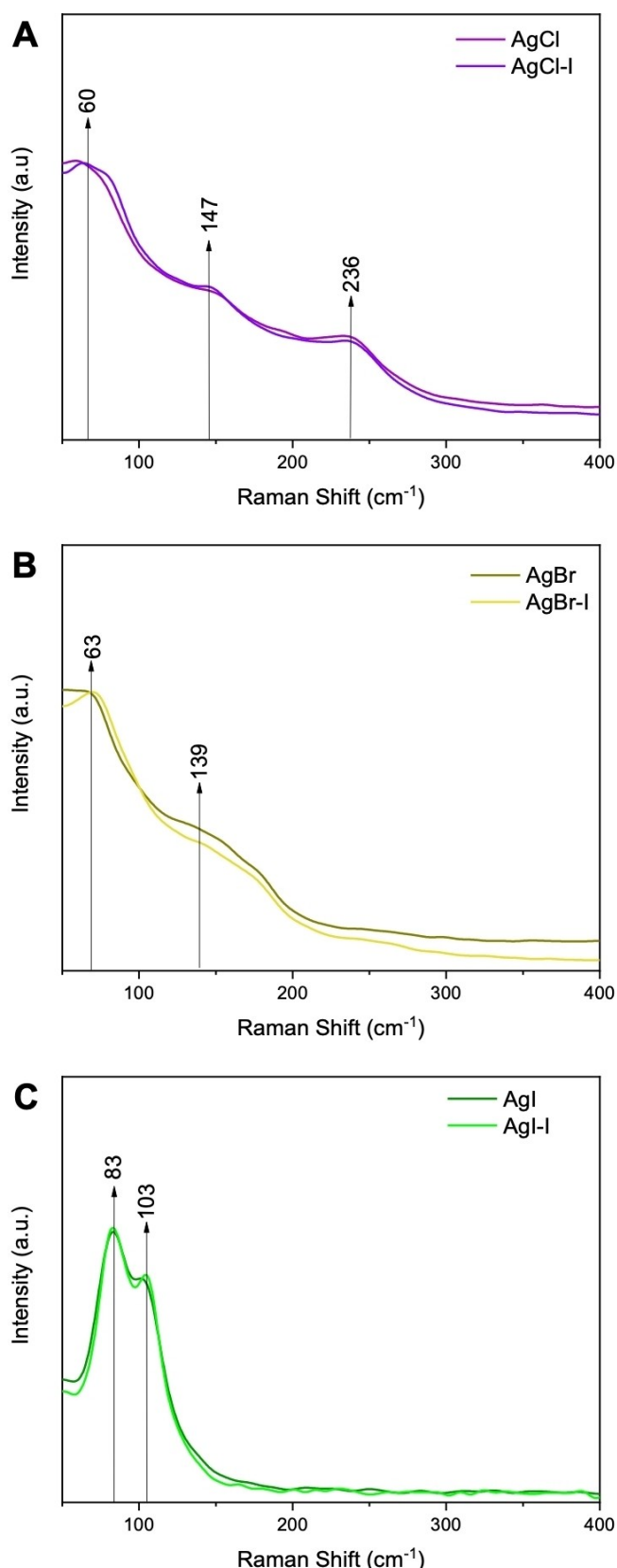European Chemical
Societies Publishing

Figure 2. Micro-Raman spectra for the samples of (A) AgCl, (B) AgBr and (C) AgI before and after irradiation with electron beam. Index I refers to the irradiated material.

irradiation are lower than those reported in the literature (2.83, 2.48, and 2.71 eV for AgCl, AgBr, and AgI, respectively). This is due to a higher degree of structural disorganization in the materials prepared using the CP method. When the materials are subjected to electron beam irradiation, an increase in the E_{gap} value of 3.12, 2.67, and 2.97 eV for AgCl, AgBr, and AgI, respectively was observed, which is much closer to those reported in the literature.[103,104] This increase was attributed to the higher degree of structural ordering in the materials, because when irradiated, the sample receives energy from the electron beam causing the electronic levels from defects in the prohibited band gap region to disappear, thus increasing the E_{gap} value. These defects can be seen by the inclination of an Urbach tail[105] in the electronic transition, which is related to the distortions in the $[AgX_y]$ (X=Cl, Br and I, Y = 6 (for Cl and Br) and 4 (for I)) clusters. In the case of AgI, the E_{gap} value obtained for this sample is very close to that for the hexagonal phase (β-AgI) reported in the literature due to a decrease in the cubic phase (γ-AgI).

Photoluminescence (PL) measurements were performed in order to investigate the medium-range structural order and defects in the samples studied. Figure 3 shows the PL spectra of the irradiated and non-irradiated AgX (X=Cl, Br, and I) samples obtained using the CP method. For all the samples, a broad band emission in the visible light region was observed, which is typical for multiphonon processes. Therefore, the recombination process of the electron-hole (e'-$h^\bullet$) pairs occurs via several pathways due to the presence of intermediate energy levels within the band gap generated by the structural order-disorder effects, which are in a pre-excited state, leading to relaxation of the electron momentum via phonon emission on the lattice over a wide range of energy.[106–108]

For the irradiated samples, no change in the emission profile was observed in relation to the non-irradiated samples. Table 1 shows the relation of the deconvolution areas of the total emission curve using the Voight function. The AgCl samples were deconvoluted from the curves centered at wavelengths of 548.3, 601.8, and 653.3 nm; AgBr at 550.5, 601.0, and 646.0 nm; and AgI at 553.7, 608.2, and 646.0 nm. It was observed that the percentages of the deconvolution have small variations that are not significant, maintaining the permanence of the emission profile observed for the materials. A decrease in the intensity of the PL was observed when the sample was subjected to electron beam irradiation. Since the PL emission was attributed to the structural disorder, the decrease in the PL intensity is due to an increase in the degree of structural order, as observed by XRD and ultraviolet-visible (UV-Vis) absorption spectroscopy.

2.4. Formation of Ag nanoparticles

Field emission-scanning electron microscopy (FE-SEM) was used to determine the morphology and structure of the samples. Figure 4 shows the FE-SEM images obtained for the samples, before electron beam irradiation, and their respective particle size distribution. It was observed that all the samples have deformed morphologies and exhibit a high degree of
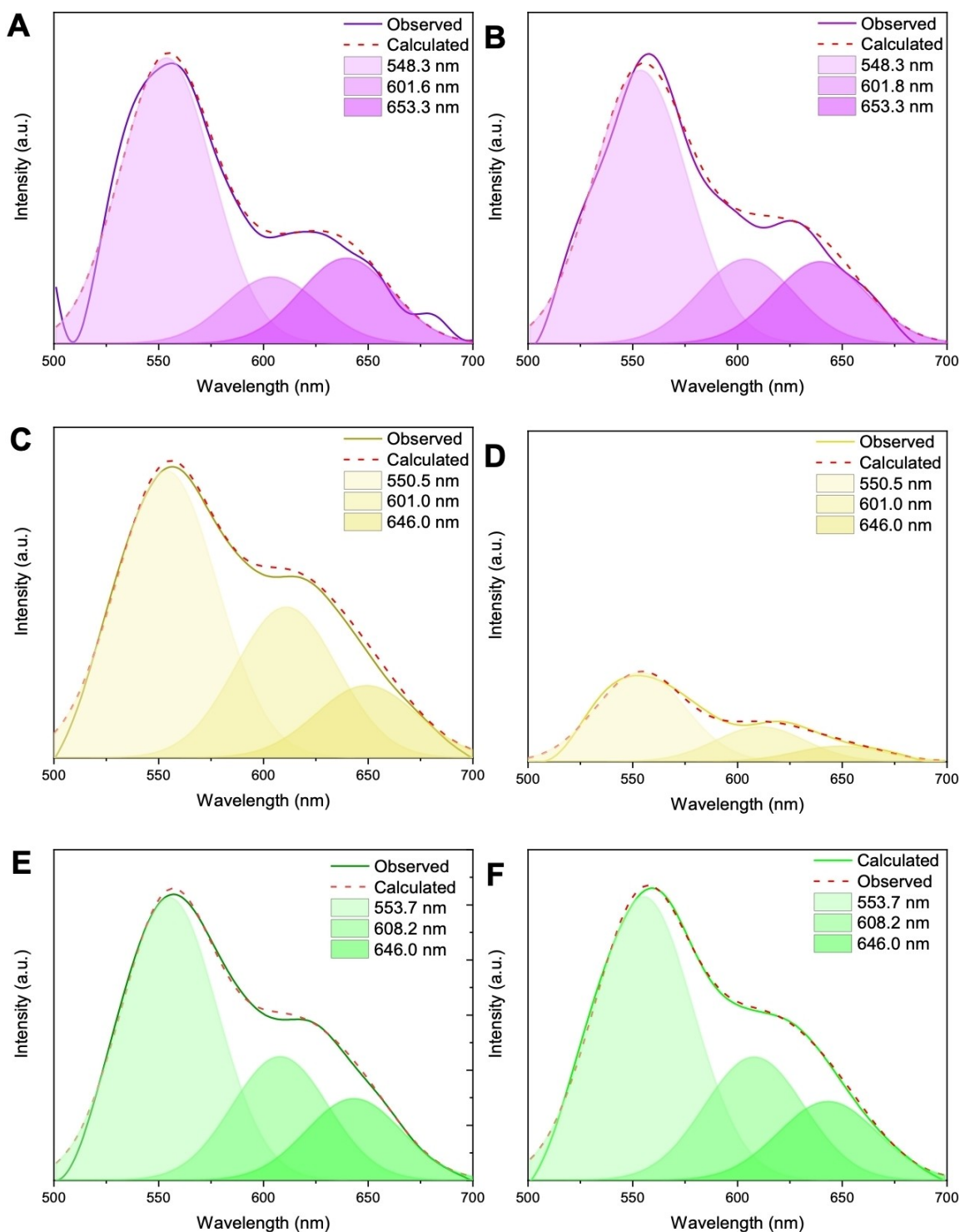
ChemistrySelect

Full Papers
doi.org/10.1002/slct.202000502

Chemistry Europe
European Chemical
Societies Publishing

Figure 3. PL spectra for the samples of the (A) AgCl, (B) AgCl–I, (C) AgBr, (D) AgBr–I, (E) AgI, and (F) AgI–I samples. Index I refers to the irradiated material.

agglomeration, with only a small number of non-agglomerated particles. The particle size distribution shows that AgCl has a larger mean size (1.013 ± 0.366 nm), followed by AgBr (0.653 ± 0.245 nm) and AgI (0.494 ± 0.157 nm).

FE-SEM was used to analyze the nucleation and formation processes of the metallic Ag nanoparticles in the different AgX

(X=Cl, Br and I) samples. With the intention of uncovering the growth of the Ag nanoparticles on the surface of the different materials, the interaction of a single particle with the electron beam was observed. Figure 5 shows this evolution from 0 to 5 min for the AgCl (Figure 5A–F), AgBr (Figure 5G–L) and AgI (Figure 5M–R) samples. The formation of small nanoparticles

ChemistrySelect

Full Papers
doi.org/10.1002/slct.202000502

Chemistry Europe
European Chemical
Societies Publishing

Table 1. Deconvolution of AgX (Cl, Br and I) samples irradiated and non-irradiated with electron beam.					
Non-Irradiated Sample			**Irradiated Sample**		
Wavelength (nm)	$\lambda = 548.3$	$\lambda = 601.8$	$\lambda = 653.3$	$\lambda = 548.3$	$\lambda = 601.8$	$\lambda = 653.3$
AgCl (%)	60.2	25.4	14.4	57.0	28.6	14.5
Wavelength (nm)	$\lambda = 550.5$	$\lambda = 601.0$	$\lambda = 646.0$	$\lambda = 550.5$	$\lambda = 601.0$	$\lambda = 646.0$
AgBr (%)	50.6	29.7	19.7	57.6	25.9	16.5
Wavelength (nm)	$\lambda = 553.7$	$\lambda = 608.2$	$\lambda = 646.0$	$\lambda = 553.7$	$\lambda = 608.2$	$\lambda = 646.0$
AgI (%)	56.7	27.9	15.4	57.6	27.8	14.6
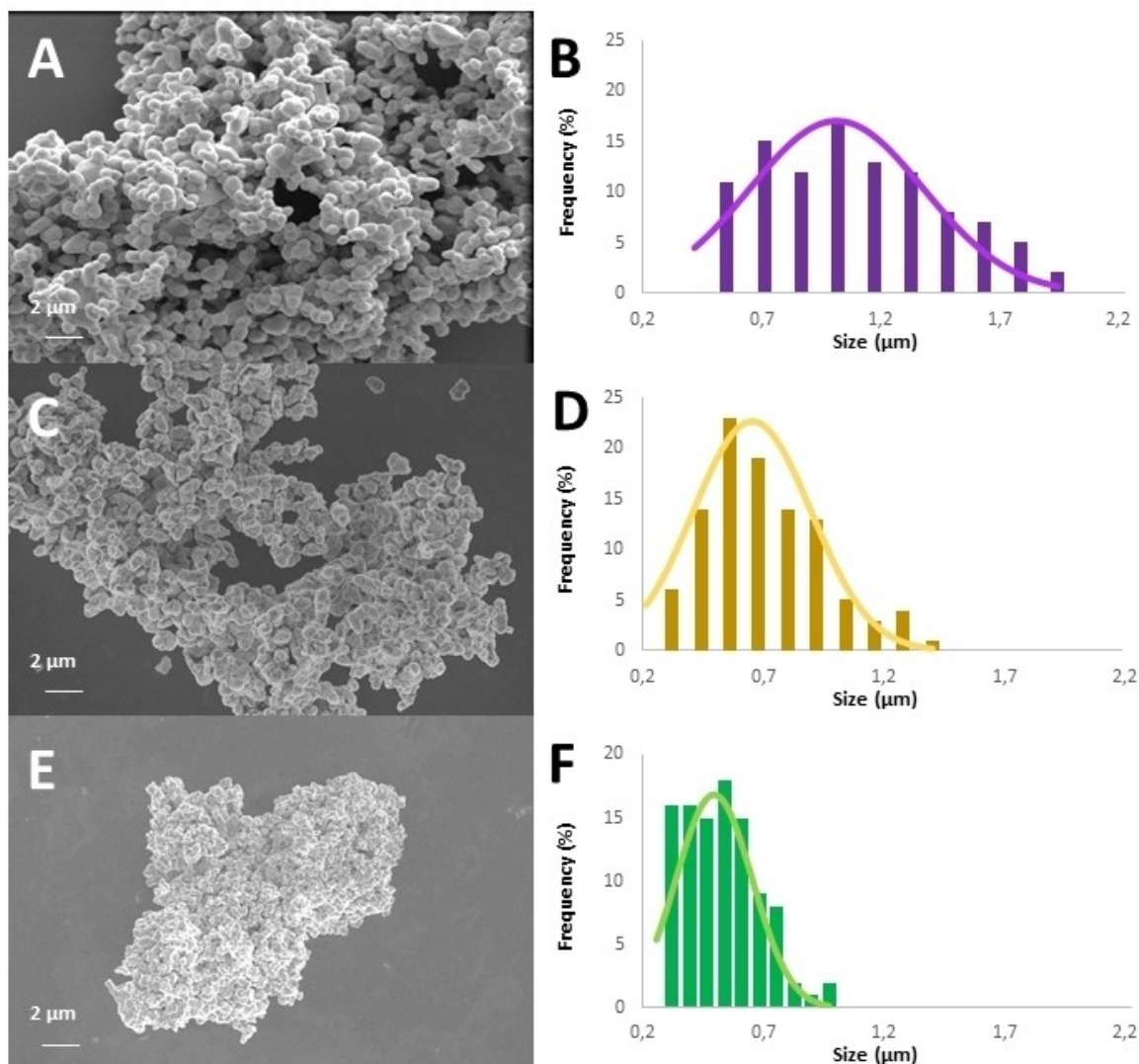
Figure 4. FE-SEM images and size distribution for the (A–B) AgCl, (C–D) AgBr and (E–F) AgI samples.

was observed for all the samples and was very similar to those obtained for silver oxides such as α-Ag$_2$WO$_4$,[68] β-Ag$_2$WO$_4$,[71] Ag$_2$CrO$_4$,[109] β-Ag$_2$MoO$_4$,[70] and β-AgVO$_3$[110] when they come into contact with an electron beam at different voltages of acceleration. It is still possible to observe that the phenomenon is different for the three AgX materials studied. Due to the polarizing power of I$^-$ being lower than Br$^-$ and consequently Cl$^-$, this causes the strength of the Ag–I bond to be weaker than that of Ag–Br and Ag–Cl. Thus, a smaller amount of Ag

nanoparticles is observed on the surface of the AgCl sample, followed by AgBr, and the formation of Ag micro-AgI. It was also observed the number of Ag nanoparticles tends to increase with time due to the increased reduction of Ag$^+$ cations from the bulk to the surface and that all of the material is degraded during this process, forming the nAg/Ag$_{1-n}$X (X=Cl, Br and I).

Transmission electron microscopy with energy dispersive spectroscopy (TEM-EDS) was performed to characterize the Ag
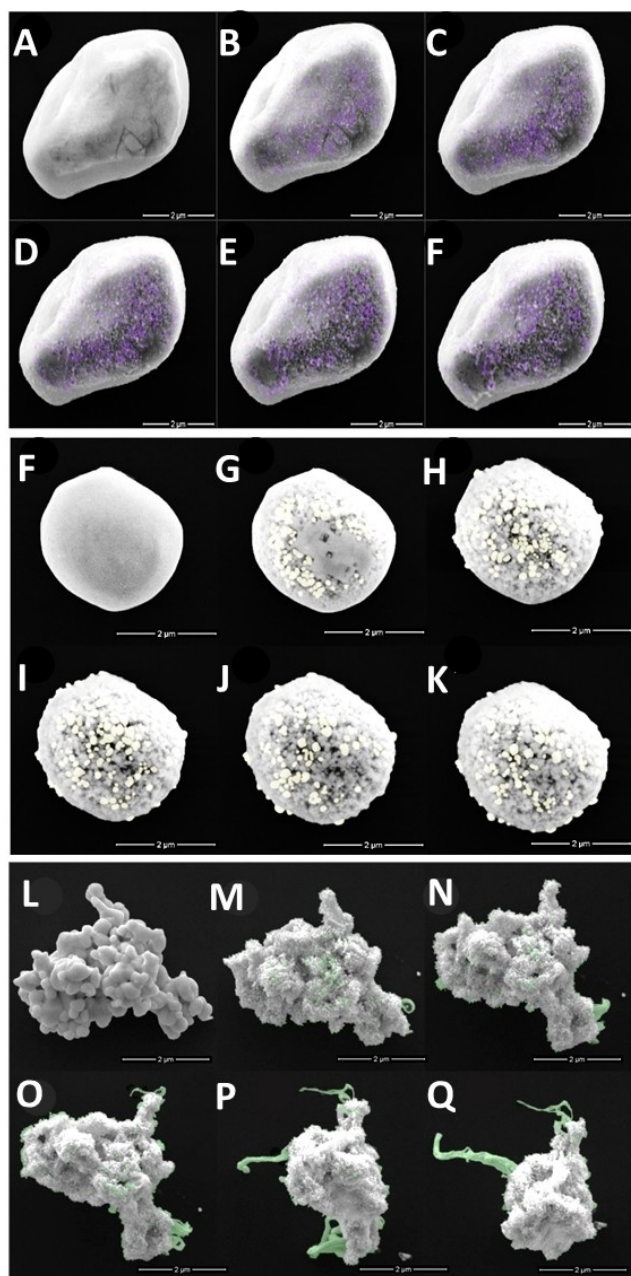
ChemistrySelect

Full Papers
doi.org/10.1002/slct.202000502

**Chemistry
Europe**
European Chemical
Societies Publishing

Figure 5. Growth of Ag nanoparticles under exposure to electron beam irradiation, at 5 kV in FE-SEM, during 1 to 5 min for the (A–F) AgCl, (G–L) AgBr and (M–R) AgI samples.

filaments. Figure 6 shows the results obtained for the AgCl (Figure 6A–C), AgBr (Figure 6D–F) and AgI (Figure 6G–H) samples. The TEM images show that the formation of the Ag nanoparticles on the surface occurs after 30s for all the materials studied. The time required to obtain the Ag nanoparticles during TEM analysis was lower because the acceleration voltage used in the equipment was significantly higher (200 kV). EDS analysis of the AgX materials (Figure 6C, 6F, and 6I) shows that the particles grown via electron beam irradiation are formed by Ag with only a few halides (Cl, Br and I) in their composition. This small concentration of halide is due to the

interface formed between the Ag nanoparticles and the matrix. Therefore, as reported by Longo et al.,[68] the formation of Ag nanoparticles occurs after electron beam irradiation of the AgX (Cl, Br and I) samples via the reduction of Ag in the semiconductor matrix.

2.5. Theoretical results

As mentioned previously, both AgCl and AgBr have a rock salt structure constructed from [AgX]$_6$ (X=Cl and Br) clusters. γ-AgI is formed in a cubic form (zinc blend) and β-AgI in a hexagonal structure, both of which are composed of [AgI]$_4$ clusters.[111] Figure 7 shows the AgX (X=Cl, Br and I) structures and it is important to notice that all of the structures are formed from four units cell, with the exception of β-AgI, which is formed from two unit cells.

Calculations on the electron injection were performed in order to understand the phenomenon caused by the electron beam on the AgX (X=Cl, Br and I) structures. For these calculations, up to 5 electrons were introduced into the [AgX]$_6$ (X=Cl and Br) clusters and [AgI]$_4$ clusters consisting of γ-AgI and β-AgI. The behaviors observed for the atomic charge, Ag—Ag and Ag—X (X=Cl, Br and I) bond lengths, and volume of the AgX (X=Cl, Br and I) structures as a function of the number of electrons (N) are illustrated in Figure 8.

An analysis of the Bader charge densities shown in Figure 8A reveals that both the Ag and X (X=Cl, Br and I) atoms have a tendency to receive electrons despite electron transfer occurring mainly on the Ag atoms. Therefore, at $N=3$ the Ag atoms in the AgI structures are almost reduced (from 0.27e to 0.00e for γ-AgI and from 0.29e to 0.01e for β-AgI), whereas the Ag atoms in the AgX (X=Cl, Br) structures exhibit a larger value of electron density (from 0.24e to 0.12e for AgCl and from 0.48e to 0.09e for AgBr). Figure 8B illustrates the evolution of the bond lengths observed for Ag—Ag and Ag—X (X=Cl, Br and I) as a function of N. These results show that the electron injection increases both bond lengths and, as a consequence, an expansion of the cell volume occurs, as illustrated in Figure 8C. From the Bader charge analysis, it was possible to calculate the charge of each [AgX$_6$] cluster for AgCl and AgBr, and the [AgI$_4$] cluster for γ-AgI and β-AgI; these values are shown in Table 2.

From Table 2, we can see the [AgI$_4$] clusters present a low electronic density during the neutral stage ($N=0$), whereas the [AgCl$_6$] and [AgBr$_6$] clusters present a higher value of negative charge. The low electronic density in γ-AgI and β-AgI has, as a consequence, a higher hole density in their structure. So, the distribution of electron-hole pairs in the structure is more

Table 2. Bader charge of the clusters into each AgX (X=Cl, Br and I) structure.

N	AgCl [AgCl$_6$]	AgBr [AgBr$_6$]	γ-AgI [AgI$_4$]	β-AgI [AgI$_4$]
0	−2,71	−2,41	−0,86	−0,86
3	−5,10	−4,89	−3,00	−3,00
5	−6,07	−4,08	−3,98	−4,01

ChemistrySelect

Full Papers
doi.org/10.1002/slct.202000502

Chemistry
Europe
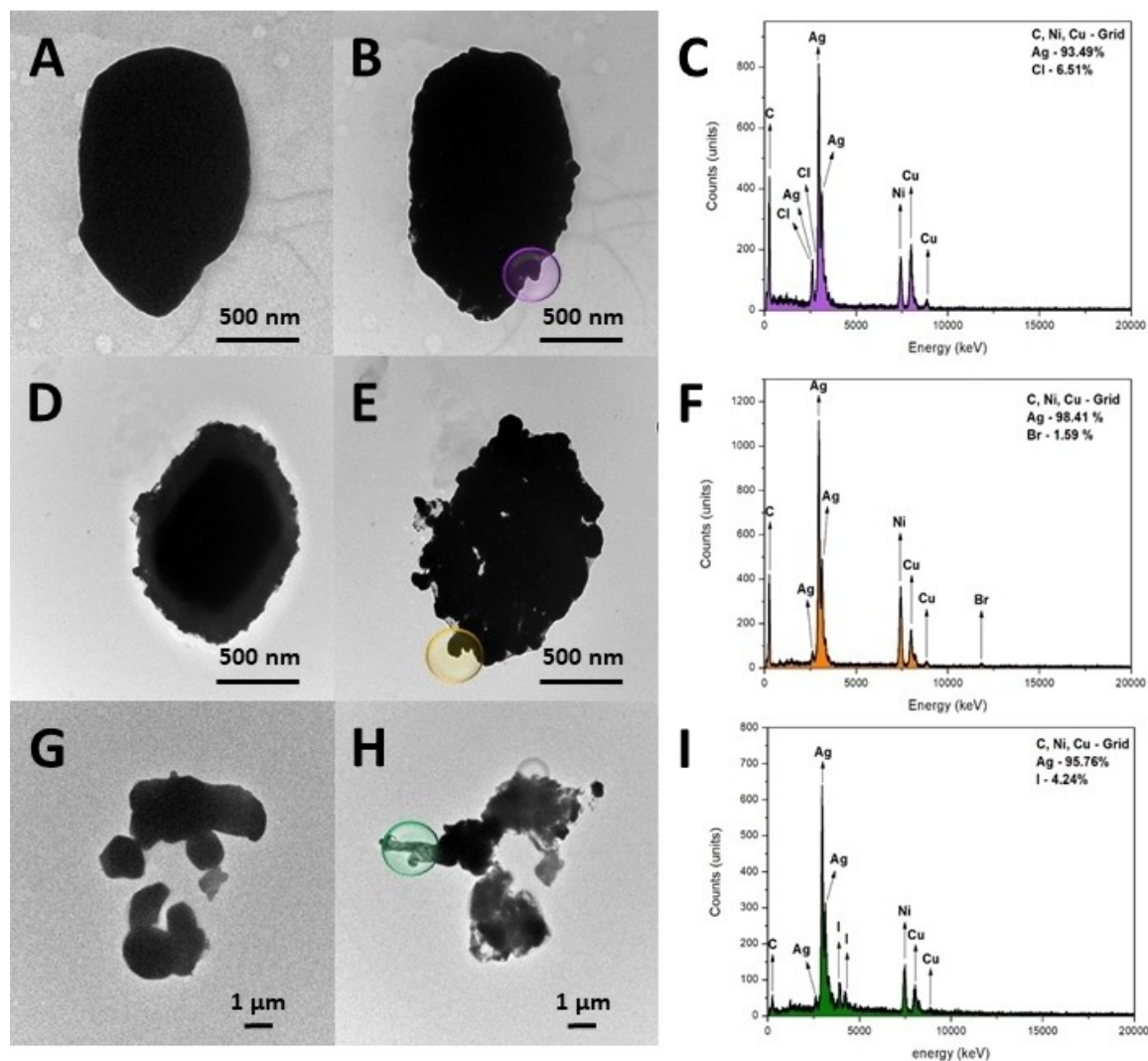European Chemical
Societies Publishing

Figure 6. TEM images of the growth of Ag nanoparticles under exposure to electron beam irradiation at 200 kV with EDS spectra for the (A–C) AgCl, (D–F) AgBr and (G–I) AgI samples.

efficient in this material, which will affect its properties, as will be shown below.

The calculation results for the charge density (ρbcp) at the (3,-1) bond critical points (BCPs), and the Laplacian of the charge density ($\nabla^2\rho_{bcp}$) in the Ag–X bonds of the [AgX]$_6$ (X=Cl and Br) and [AgI]$_4$ clusters for β-AgI and γ-AgI are listed in Table 3. The effect of electron injection to the AgX (X=Cl, Br,

and I) structures produces a notable difference in the charge density values and Laplacian. Remarkably, the charge density and Laplacian values of the Ag–X bonds decrease when the electrons are injected into the structure, which indicates that these bonds become weaker, favoring the formation of metallic Ag from the clusters. This effect is more pronounced in the [AgI]$_4$ clusters of the γ-AgI and β-AgI structures, where the reduction process takes place first.

In this way, the electrons cause a structural change in all the AgX (X=Cl, Br and I) lattices and, as a consequence, the Ag–X (X=Cl, Br and I) bonds break and the clusters suffer distortions, generating ideal conditions for the growth of Ag nanoparticles on their surfaces. It is important to note that despite the structural differences in the γ-AgI and β-AgI polymorphs, both present the same behavior upon electron injection. Therefore, it is possible to conclude that the presence of the cubic phase in the AgI sample does not affect the

Table 3. Charge density at the (3,–1) bonds critical points (ρ_{bcp}) and its Laplacian ($\nabla^2\rho_{bcp}$) in the Ag–X (X=Cl, Br and I) bonds as function of injection of electrons (N) into the structures.

	AgCl Ag–Cl		AgBr Ag–Br		γ-AgI Ag–I		β-AgI Ag–I	
N	ρ_{bcp}	$\nabla^2\rho_{bcp}$	ρ_{bcp}	$\nabla^2\rho_{bcp}$	ρ_{bcp}	$\nabla^2\rho_{bcp}$	ρ_{bcp}	$\nabla^2\rho_{bcp}$
0	0.21	2.10	1.19	-15.68	0.71	-7.00	0.28	1.59
3	0.03	0.24	1.20	-15.91	0.05	0.29	0.72	−6.66
5	0.02	0.16	0.02	0.12	0.03	0.16	0.73	−7.84

ChemistrySelect

Full Papers
doi.org/10.1002/slct.202000502

Chemistry
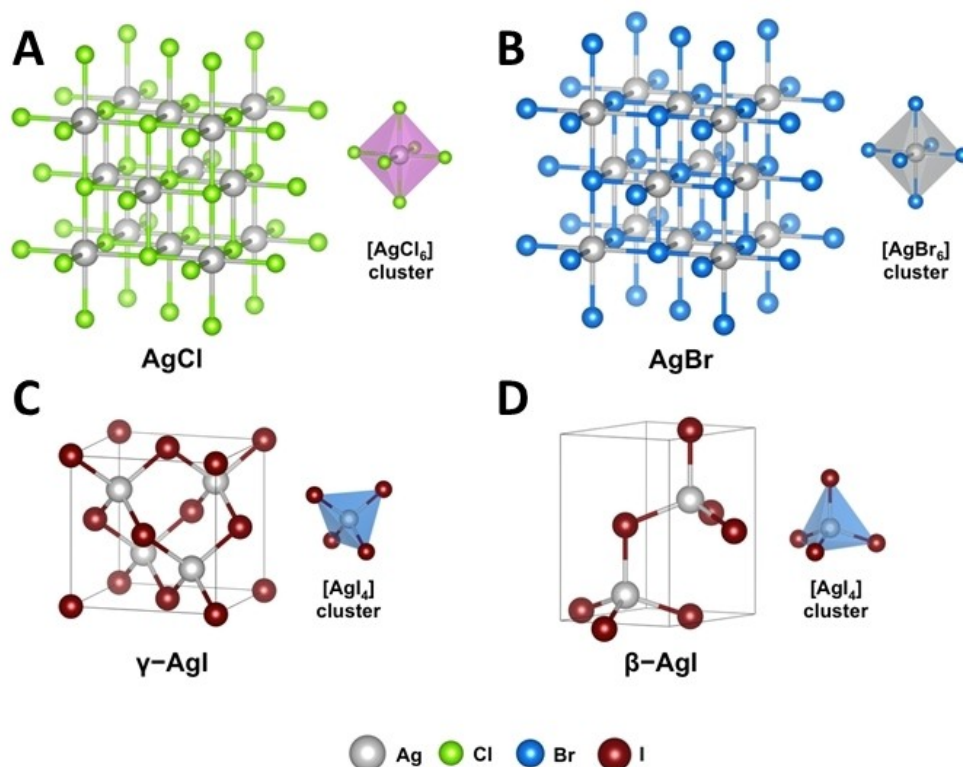Europe
European Chemical
Societies Publishing

Figure 7. Unit cell representation for the rock salt structures of (A) AgCl and (B) AgBr, (C) the zinc blend structure of γ-AgI, and (D) hexagonal structure of β-AgI.

properties, despite the disappearance of the phase after electron beam irradiation, which was observed experimentally.

Figure 9 presents the two-dimensional charge density maps associated with the interaction between the bonds of the Ag and X (X=Cl, Br and I) atoms in the AgX (X=Cl, Br and I) structures, considering the neutral state ($N=0$) and the addition of 5 ($N=5$) electrons. The isolines around the atoms specify the concentration of high and low charge density zones. From the analysis of the results displayed in Figure 9, it is possible to see that prior to electron injection ($N=0$), the isolines are equally distributed between the atoms in all the structures, whereas after electron injection ($N=5$), the same isolines are distributed closer to the Ag nuclei. This result confirms the Bader charge analysis.

2.6. Photocatalytic property

The photocatalytic activity of the non-irradiated AgX (X=Cl, Br and I) and irradiated AgX–I (X=Cl, Br and I) samples were investigated during the degradation of Rhodamine B (RhB) under visible light irradiation. RhB shows a characteristic peak located at 556 nm relative to the xanthene ring, which is its conjugated chromophore[112] that under goes a hypochromic displacement of absorption due to the action of light via de-ethylation of the *N,N′*-diethylammonium functional groups.[78] Aliquots were collected at different times (0, 2, 4, 6, 8, 10, 15, 20, 25, 30, 40, 50, 60, 75, and 90 min) during the exposition of

visible light irradiation, which were analyzed using UV-Vis spectroscopy. The results are shown in Figure SI-2. The variations in the concentration of RhB (C/C_0) versus irradiation time when in contact with the samples and the –ln of the variation in the concentration (C/C_0) of RhB versus irradiation time are shown in Figure 10, where C is the concentration at time t (min) and C_0 is the initial concentration.

For the non-irradiated materials, it was observed that the photocatalytic efficiency of AgCl was 61% and when irradiated with the electron beam this increased to 83%. Similar behavior was also observed for AgBr with the photocatalytic efficacy of the material against RhB increasing from 68 to 85%. For AgI, the increase was not as significant (from 86 to 91%), since it already exhibits a very high photoactivation activity against RhB. An analysis of the results of Figure 10 renders that the rate constant, corresponding to the slope of –ln (C/C_0) *versus* time for non- and irradiated samples, increases from 1.07×10^{-2} to 2.18×10^{-2} for AgCl and 1.14×10^{-2} to 2.09×10^{-2} for AgBr, respectively, while increases slightly from 2.29×10^{-2} to 2.56×10^{-2} at non-and irradiated sample of AgI.

Many studies have shown that reactive oxygen species (ROS), such as hydroxyl radicals (OH*), singlet oxygen ($^1O_2$), and hydroperoxyl radicals (HOO*), are responsible for the photocatalytic activity of semiconductors, which are photo-induced by holes and electrons ($h^\bullet$ and $e^{'}$, respectively).[79,113,114] According to Rehan et al.[115] and Ma et al.,[116] silver halides have the capacity to produce all reactive oxygen species, in addition to
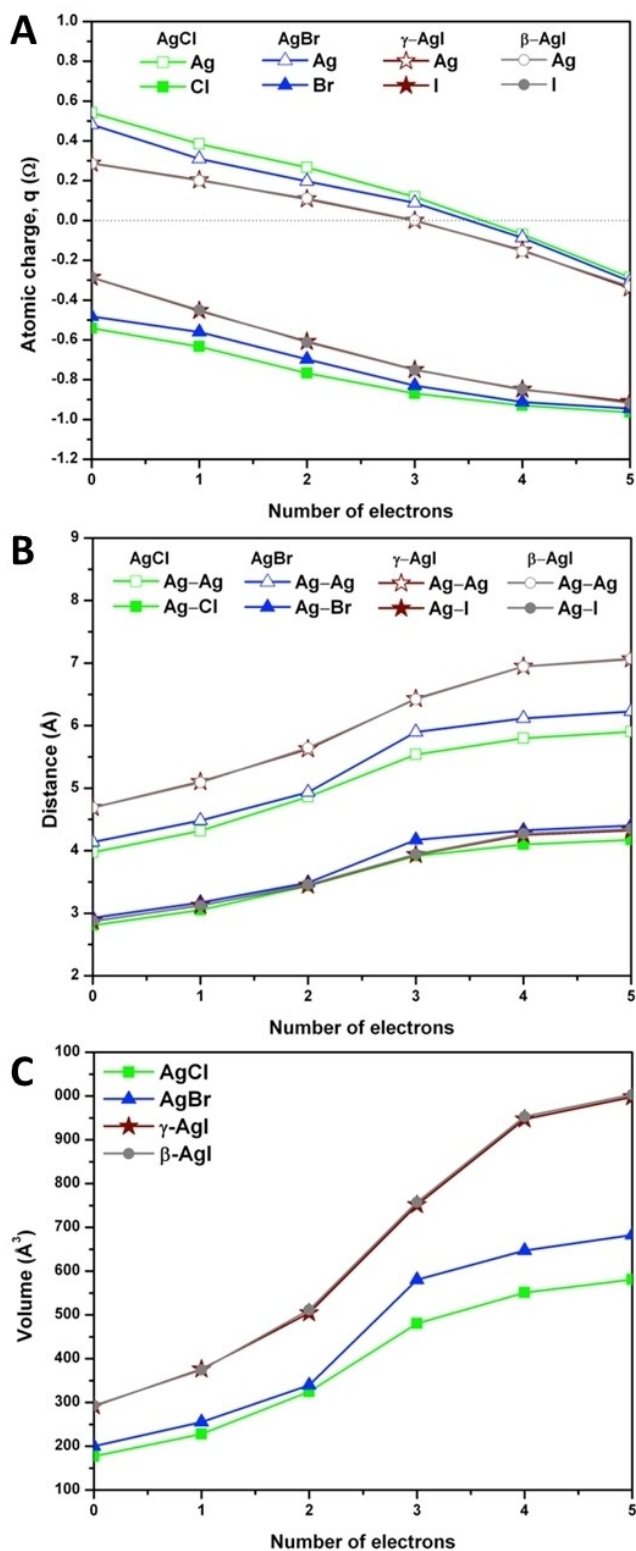
ChemistrySelect

Full Papers
doi.org/10.1002/slct.202000502

Chemistry Europe

European Chemical
Societies Publishing

Figure 8. (A) Atomic charge, q(Ω) (B) Ag—Ag and Ag—X (X=Cl, Br and I) bond lengths, and (C) volume of the AgX (X=Cl, Br and I) structures as function of the number of electrons (N).
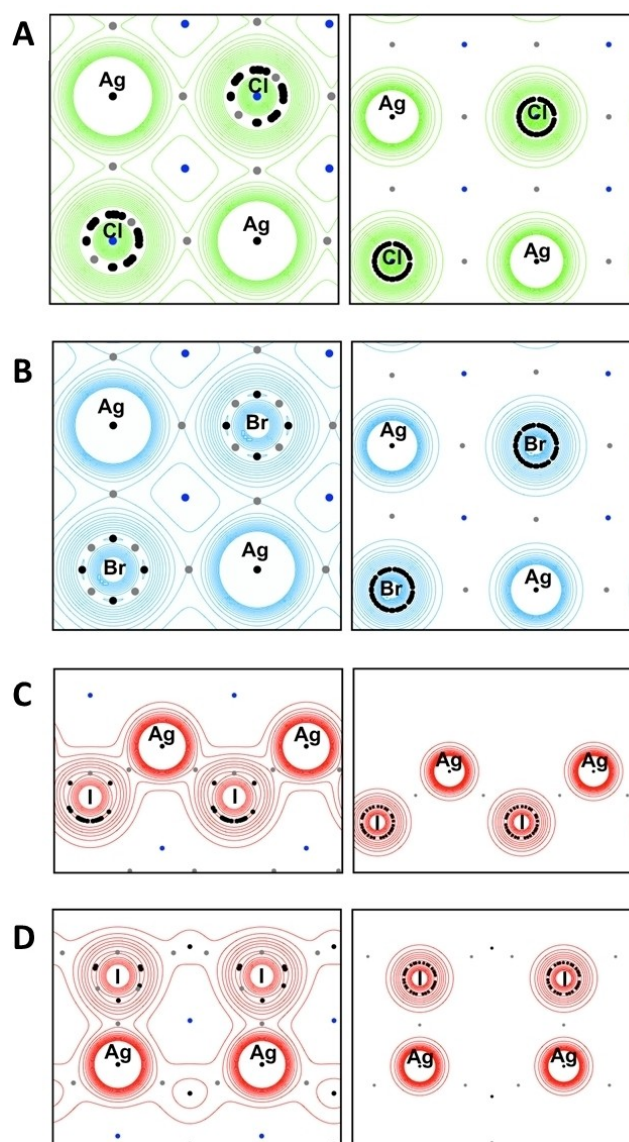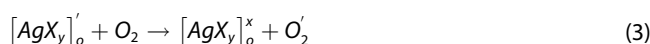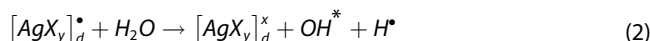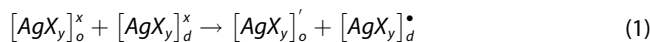

Figure 9. 2D charge density maps obtained for the AgX (X=Cl, Br and I) structures as a function of the number of electrons (N), in which is illustrated the results for N=0 and N=5 for: (A) AgCl, (B) AgBr, (C) γ-AgI, and (D) β-AgI.

their photo-inducers. Therefore, for these materials, the generation of oxygen species follows the mechanism shown below (Equations 1–3):

$$\left[AgX_y\right]_o^x + \left[AgX_y\right]_d^x \rightarrow \left[AgX_y\right]_o^{'} + \left[AgX_y\right]_d^{\bullet} \qquad (1)$$

$$\left[AgX_y\right]_d^{\bullet} + H_2O \rightarrow \left[AgX_y\right]_d^x + OH^* + H^{\bullet} \qquad (2)$$

$$\left[AgX_y\right]_o^{'} + O_2 \rightarrow \left[AgX_y\right]_o^x + O_2^{'} \qquad (3)$$

where X=Cl, Br, and I, and y=6 for Cl and Br, and 4 for I. The superscripts means: x=neutral charge; $'$=electron and $\bullet$= hole, according to the Kröger-Vink notation and the subscripts o and d means ordered and disordered, respectively.

ChemistrySelect

Full Papers
doi.org/10.1002/slct.202000502

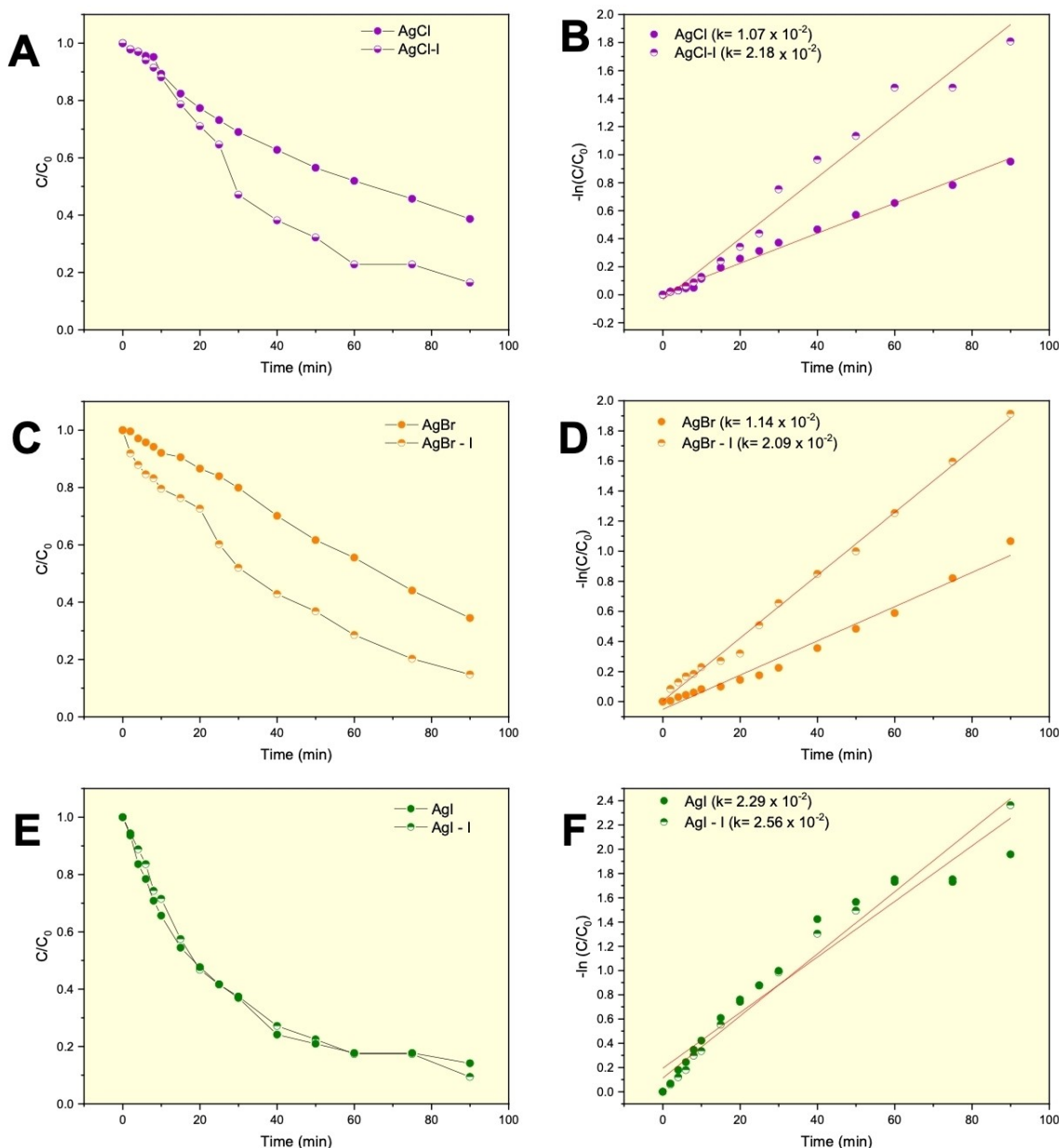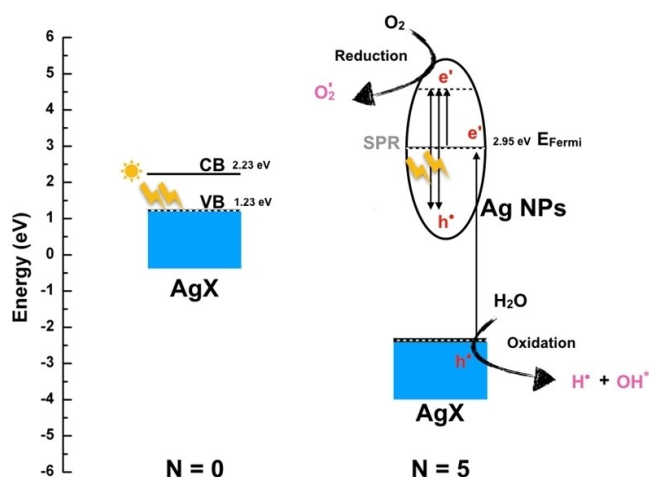**Chemistry Europe**
European Chemical
Societies Publishing

Figure 10. Relative concentration of RhB dye (C/C0) versus time (min) and reaction kinetics of RhB degradation -ln(C/C0) versus time (min) of the (A–B) AgCl, (C–D) AgBr and (E–F) AgI sample. Index I refers to the irradiated material.

When metallic Ag nanoparticles are on the surfaces of the AgX materials, a Schottky barrier is established at the interface between Ag nanoparticles and AgX. The Fermi level of the Ag nanoparticles is higher than that of AgX.[117] When the Ag/AgX photocatalyst is irradiated with visible light, the free electrons in the lowest unoccupied orbital of Ag nanoparticles are excited to higher energy states due to the SPR effect.[118] Therefore, the free electrons can easily transfer to the CB of AgX and are then trapped by surface-absorbed oxygen molecules or water to form $^1O_2$ or OH^*.[119] Meanwhile, the $h^\bullet$ in the highest occupied orbital of Ag nanoparticles cannot only directly oxidize organic dyes such as RhB, but can also be transferred to the AgX surface and cause the oxidation of X^- to

X^0. Because X^0 is a reactive radical species, RhB can be oxidized by X^0 and hence it is reduced back to X^-. Therefore, the Ag/AgX photocatalyst slows down the recombination process between the $h^\bullet$ and $e^{'}$, maintaining the stability in the photocatalytic process. In summary, the SPR of uniformly distributed Ag nanoparticles, the quality of AgX, and well-defined interface between Ag nanoparticles and AgX can be assumed to enhance the photocatalytic efficiency and stability.

Based on the above analysis, we proposed the photo-catalytic mechanism for the Ag nanoparticle/AgX materials using the Z-scheme shown in Scheme 1. The photocatalytic process can take a place in the three following steps; i) Firstly, the Ag nanoparticles generated upon electron beam irradiation

ChemistrySelect

Full Papers
doi.org/10.1002/slct.202000502

**Chemistry
Europe**
European Chemical
Societies Publishing

Scheme 1. Schematic energy band alignment diagram (within the Z-scheme) for the proposed photocatalytic mechanism of Ag nanoparticles/AgX (X=Cl, Br and I).

$$AgX + h\nu \rightarrow AgX \ (e^{'} + h^{\bullet}) \tag{4}$$

$$\text{Plasmonic Ag nanoparticles} \rightarrow$$
$$\text{Enhanced charge separation} \ (e^{'} + h^{\bullet}) \tag{5}$$

$$O_2 + e^{'} \rightarrow O_2^{'} \tag{6}$$

$$H_2O + h^{\bullet} \rightarrow H^{\bullet} + OH^{*} \tag{7}$$

$$H^{\bullet} + O_2^{'} \rightarrow \ O_2H^{*} \tag{8}$$

$$O_2^{'} + h^{\bullet} \rightarrow \ ^1O_2 \tag{9}$$

$$O_2H^{*} + OH^{*} + {}^1O_2 + \text{Pollutants} \rightarrow \text{Degradation products} \tag{10}$$

absorb visible light for creating charge-separated $h^{\bullet}$ and $e^{'}$ via the SPR effect, and the energy of these electrons can be excited to ~2.95 eV above their Fermi level; ii) redox equivalents (mobile electrons and holes) are generated and subsequently migrate to catalytic centers. Then, the energetic electrons in the Ag nanoparticles overcome the Schottky barrier at the metal-semiconductor interface allowing electron transfer to occur to the conduction band of AgX, leaving energetic holes in the Ag metal, i.e. the holes formed on the Ag nanoparticles recombine with the photoinduced electrons from the AgX semiconductor. iii) redox equivalents which in turn interact with substrates at the reactive centers. Thus, the hot electrons in the semiconductors will drive the reduction reactions and the hot holes in the metal will drive the oxidation reactions. Then it could be ascribed that, an excellent photocatalyst must be strong absorber of sunlight, exhibit a long lifetime of excited state, high yield of charge separated states, and characterized by good charge mobility.

As shown in Scheme 1, there is an electron flow between the metallic Ag and the VB of AgX that combine with the holes in Ag. Therefore, a large number of electrons are accumulated on the surface of the Ag nanoparticles and the photo-generated electrons capture O_2 to generate $O_2^{'}$, i.e. the absorbed molecular oxygen can be easily reduced to $O_2^{'}$ at the solid interface of the catalyst by the photo-generated hot electrons. Moreover, it also can be transformed into H_2O_2 and then form into OH^{*} through multi-step reduction reactions. The maintained photogenerated holes of the Ag nanoparticles with high oxidation ability can directly react to decompose H_2O into OH^{*} and $H^{\bullet}$. The remaining holes can directly oxidize $O_2^{'}$ into $^1O_2$, which is crucial for the photocatalytic degradation process. Therefore, $^1O_2$, OH^{*} and $H^{\bullet}$ are responsible for the photodegradation processes of pollutants. The complete mechanism involving the different electron transfer processes of the hot charge carriers can be summarize as follows (Equations 4–10):
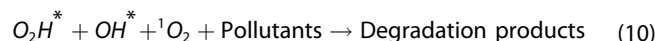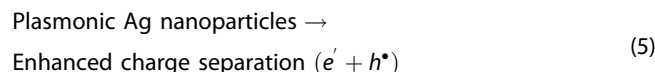
In general, the efficient Z-scheme heterojunction can optimize the redox ability of the photocatalyst and lead to superior photocatalytic performance.[120,121]

In order to evaluate the photocatalytic stability against RhB, four photocatalytic cycles were performed reusing the materials. Figure 11 shows the results obtained. For all materials, irradiated or not, a tendency to linear decrease in the photocatalytic activity was observed, which was more pronounced for AgBr and AgCl. This decrease in the photocatalytic activity was due to the structural and morphological changes that occur in Ag-based materials due to the degradation in their composition during the formation of other species. This happens because semiconductors that present an E_{gap} in the near-ultraviolet region, which are more susceptible to photocorrosion, and causes the active sites of the materials to be covered by the new species produced during the photocatalytic process.[122] In some studies of the group with Ag-based materials, it was possible to observe the formation of Ag^0 and Ag-based oxides during the photocatalytic cycles, and that depending on the concentration of these species, at first a slight increase in the photocatalysis, followed later by a decrease in photocatalytic efficiency due to degradation of the Ag-based material.[79] Since the AgX (X=Cl, Br and I) solubility constant follows the order-AgCl (1.77×10^{-10}) > AgBr (5.35×10^{-12}) > AgI (8.52×10^{-17})-AgCl and AgBr are more susceptible to photocorrosion and the loss of efficiency during the photocatalytic cycles being more pronounced for these materials.[123] These results show that electron beam irradiation can be used as a tool to increase the rate of photodegradation, which was evidenced by the reaction kinetics shown in Figure 10, which reduces the loss of efficiency during the cycles of use of the photocatalyst, increasing its useful life (Figure 11).

2.7. Zebrafish tests

Fish models have been frequently used to test the toxicity and environmental risks of materials because they can be used to evaluate important parameters such as the mortality, compartment alterations, defects, and modifications in tissues, cells, and genetic material under controlled conditions, from which it is possible to predict their adverse effects.[124] As shown in previous work,[125] some material characteristics, such as the
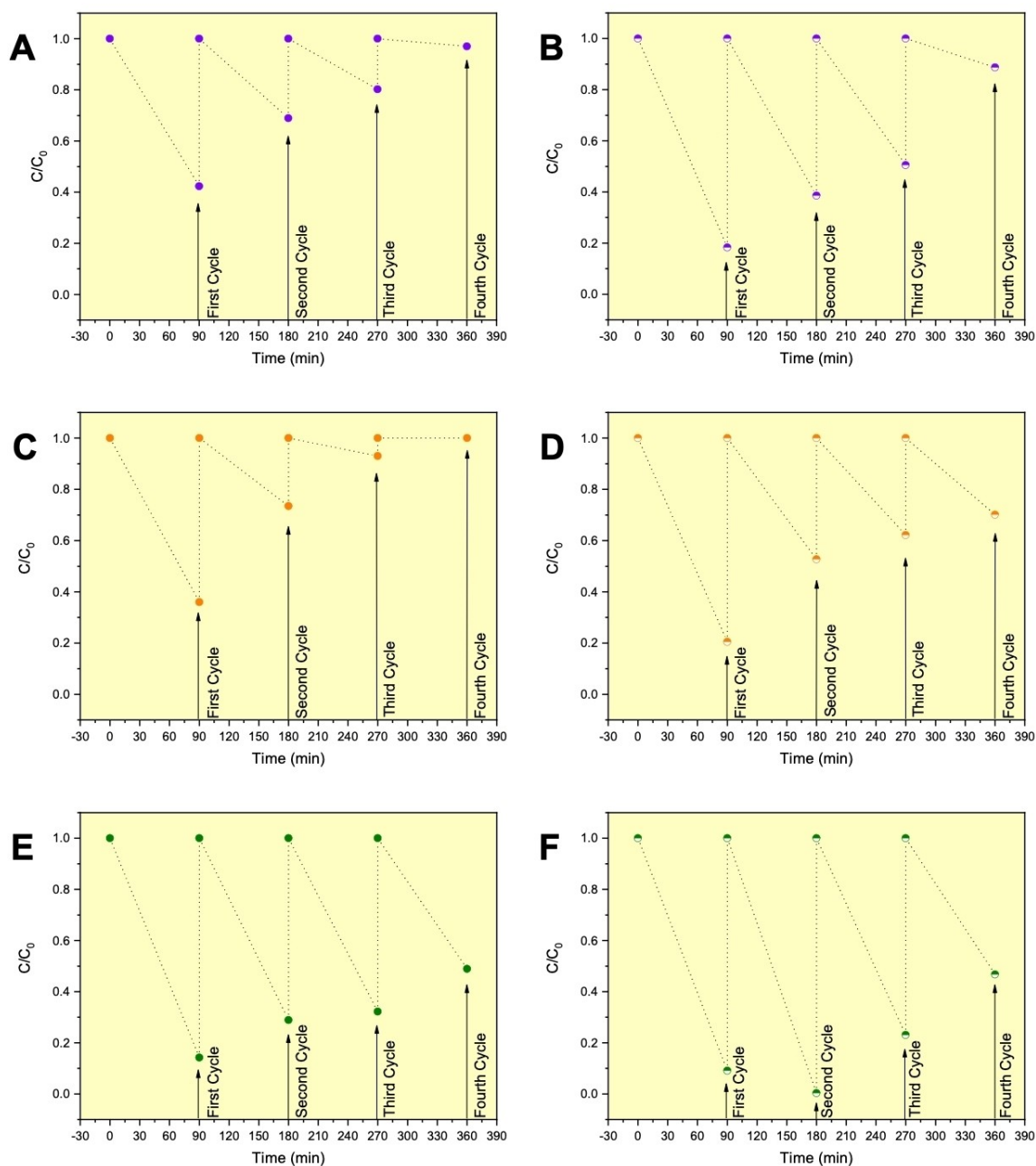
ChemistrySelect

Full Papers
doi.org/10.1002/slct.202000502

Chemistry Europe
European Chemical
Societies Publishing

Figure 11. Recycling runs for RhB photodegradation over the (A) AgCl, (B) AgCl–I, (C) AgBr, (D) AgBr–I, (E) AgI, and (F) AgI–I samples under visible light irradiation.

particle sizes, morphology, and solubility, may be the main causes of the different forms of interaction with biological molecules, such as membrane proteins and genetic material. For this purpose, the toxicity of some materials has mainly been related to the dispersion capacity of Ag nanoparticles in an aquatic environment because at low doses, Ag nanoparticles can exhibit algicidal, fungicidal, and bactericidal properties.[126] In our study, the AgCl, AgBr and AgI samples were tested because their widespread use by industry and discharge into the environment may have an impact on a wide variety of aquatic organisms as well as human health.[127,128]

In the present work, the toxicity of the non-irradiated and irradiated AgCl, AgBr and AgI samples were analyzed upon being exposed to zebrafish embryos for 120 h at concentrations of 0.125, 0.25, 0.5, 1, and 2 mg/mL. The embryo survival data were recorded every 24 h of exposure to the samples and verified in the presence of the following morphological changes: Somite formation, the incidence of pericardial edema, heartbeat, malformations of the spine, tail, and head, body length from muzzle to the tip of the tail, yolk sac length, and developmental delay.

ChemistrySelect

Full Papers
doi.org/10.1002/slct.202000502

Chemistry Europe
European Chemical
Societies Publishing

For the AgCl (Figure 12A), AgCl-I (Figure 12B), AgBr (Figure 12C), and AgBr-I (Figure 12D) samples, the embryonic survival did not exceed the first 5 h of exposure, causing 100% mortality. When exposed to the AgI (Figure 12E) and AgI-I (Figure 12F) samples at all the concentrations tested, the embryos remained viable after 120 h of exposure, the survival rates were equivalent to the control group, and there were no morphological changes (Figure 13).

The results obtained in relation to the survival rate of the embryos may be related to the solubility to the materials. According to Lee et al.,[129] the high solubility of certain materials may lead to the release of Ag nanoparticles, which

allows their entry through the channels of the chorion in zebrafish embryos and thus, produce detrimental effects on embryonic development. The AgCl and AgBr materials show high toxicity toward the embryos (100% mortality) because at low concentrations in water they display greater solubility when compared to AgI [AgCl (1.77×10^{-10}) > AgBr (5.35×10^{-12}) > AgI (8.52×10^{-17})],[123] which was in accordance with the results obtained by Lee et al..[129] The results presented for the three samples are equivalent to the samples irradiated with electrons, suggesting that electron beam irradiation did not alter the effects caused by the materials analyzed.
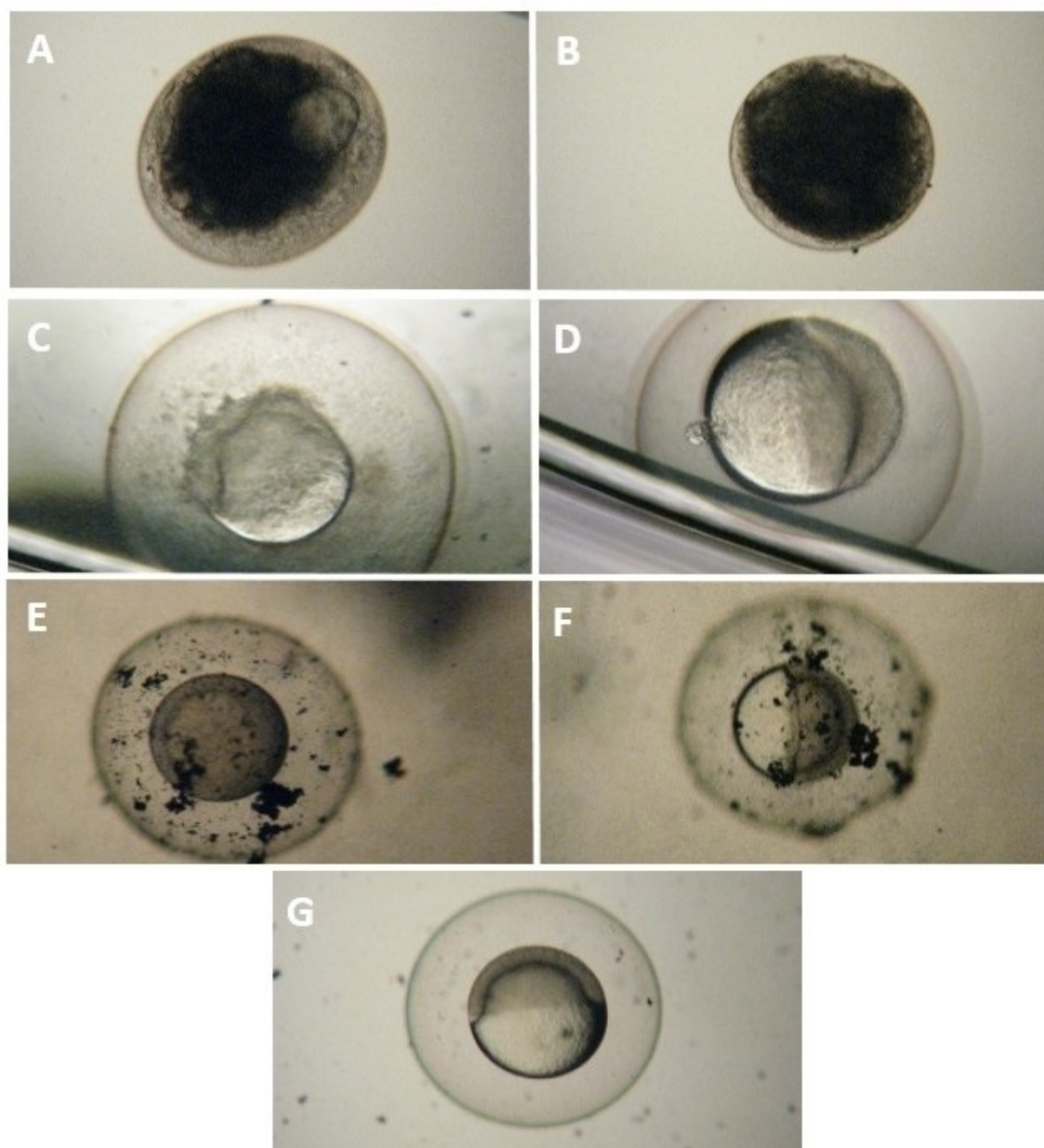

Figure 12. Impact on the development of zebrafish embryos exposed for 5 h in the respective samples. (A) AgCl; (B) AgCl–I; (C) AgBr; (D) AgBr–I; (E) AgI; (F) AgI–I (G) control.

ChemistrySelect

Full Papers
doi.org/10.1002/slct.202000502

Chemistry
Europe
European Chemical
Societies Publishing

Figure 13. Development of zebrafish embryos exposed to higher concentrations of AgI and AgI–I at 24, 48, 72, 96, and 120 h, respectively.

As shown in Figure 12A–B, AgCl in both its non-irradiated and irradiated forms showed toxicity toward the embryos. Groh et al.,[130] also observed similar results when analyzing zebrafish embryo exposure under the influence of Cl⁻ on Ag⁺ availability.

ChemistrySelect

Full Papers
doi.org/10.1002/slct.202000502

Chemistry
Europe
European Chemical
Societies Publishing

According to the authors, a high Cl⁻ content in the medium dramatically increased the toxicity of the sample, limiting the viability of the organisms studied. Recently, Iniyan et al.[131] also studied zebrafish embryos exposed to AgCl and demonstrated that a 1000-fold lower dose of the concentration used in this study was able to cause neurological, cardiac, and yolk sac damage, which indicated that significantly smaller amounts of AgCl are sufficient enough to influence the development of the embryos. Although chlorine is present in the aquatic environment and exerts a number of biological functions, such as ion exchange through the chlorine channels in fish,[132] increasing the concentration of chloride in the aquatic environment can result in osmotic stress[133] and, in turn, requires the excessive energy expenditure of organisms, which can lead to death.

In addition to AgCl, the AgBr samples showed highly toxic to zebrafish embryos (Figures 12C–D). Due to the lack of information in the literature on the analysis of this material in aquatic organisms, to the best of our knowledge, AgBr presents a biological action similar to that of AgCl, since both materials cause the mortality of zebrafish embryos in the first few hours of exposure.

Our results suggest that AgCl and AgBr may affect the embryonic development of zebrafish. As both cause high embryo mortality in the first few hours of exposure, it is clear that preventive measures should be taken in relation to the release of these materials into the environment in order to avoid risks to wildlife and human health.

Among the samples tested, AgI presents the lowest solubility in aqueous solutions[123] representing a source low in Ag⁺ and I⁻, making it biologically unavailable in the environment and therefore much less toxic or even non-toxic to a variety of species of terrestrial and aquatic animals.[134,135] Since the AgI samples showed no toxicity to the zebrafish embryos, analyzes were required to obtain information on possible tissue damage caused by the sample. In the cell death assay using acridine orange and ethidium bromide (AO/EB), we observed that larvae obtained after 120 h of exposure to the AgI sample did not present tissue death due to apoptosis or necrosis (Figure 14). This result was in accordance with those previously reported,[134] confirming that the AgI samples do not exhibit toxicity toward the embryos, since they were not able to cause damage to vital tissues and, consequently, to cause death.

3. Conclusions

Manipulating the electronic structure of a semiconductor is an ideal approach for the exploration and development of new photocatalysis and low toxicity agents. In this paper, we report the synthesis of Ag nanoparticle/AgX (X=Cl, Br and I) composites by electron beam irradiation, which as far as we know is the first time this has been carried out. First-principles calculations, at the DFT and QTAIM levels, were employed to reveal the nature of the formation of the Ag nanoparticles under electron beam irradiation. From our calculations, a Z-scheme photocatalytic mechanism has been proposed based on photo-induced charge separation and transfer. By combining the experimental and theoretical results, an in-depth
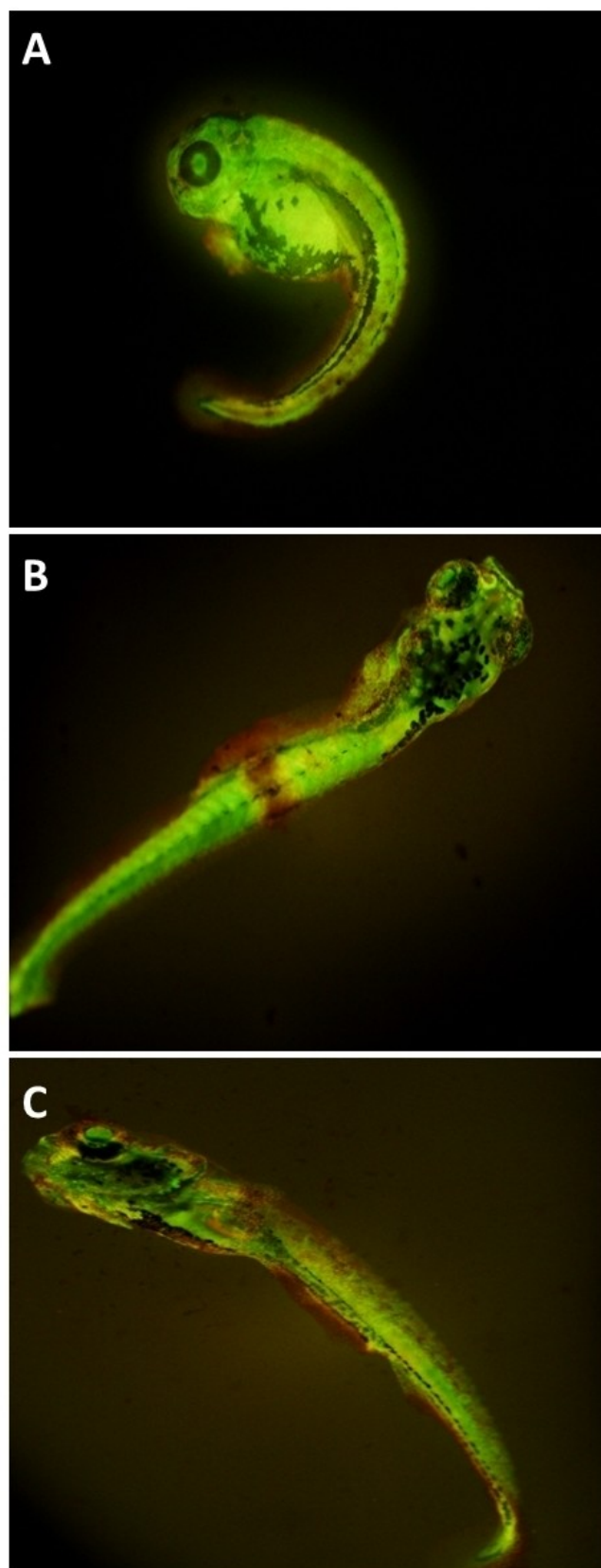

Figure 14. Cell death assay (apoptosis and necrosis). The figure shows that exposure of (A) AgI and (B) AgI–I after 120 h does not cause death to vital tissues in zebrafish larvae. (C) Presents a zebrafish larvae control.

ChemistrySelect

Full Papers
doi.org/10.1002/slct.202000502

Chemistry
Europe
European Chemical
Societies Publishing

understanding of their photocatalytic performance during the photodegradation of Rhodamine B and toxicological activity against zebrafish is presented. The outstanding properties benefit from the high dispersion of Ag nanoparticles and enhanced interactions between the Ag nanoparticles and the AgX semiconductor. This work opens up a new avenue for the one-pot synthesis of new photocatalytic and low toxicity materials that are highly effective and yet not toxic to the environment, thus closing a sustainable cycle of the process of degradation of organic pollutants. It also provides a deeper insight not only allowing us to explain the mechanism of these activities, but also to contribute to the rational design of new materials for multifunctional applications.

Supporting Information summary

All the experimental procedures concerning the synthesis, characterizations, photocatalytic evaluation, biological measurements and also the computational methods and model systems are reported in the supporting information. The ultraviolet-visible graphics are also included.

Acknowledgements

Conflict of Interest

The authors declare no conflict of interest.

Keywords: Ag nanoparticles · photocatalytic activity · silver halides · toxicological effects

[1] A. Kubacka, M. Fernandez-Garcia, G. Colon, *Chem. Rev.* **2011**, *112*, 1555–1614.
[2] C. Li, Y. Xu, W. Tu, G. Chen, R. Xu, *Green Chem.* **2017**, *19*, 882–899.
[3] X. Dai, Z. Han, G. I. N. Waterhouse, H. Fan, S. Ai, *Appl. Catal. A* **2018**, *566*, 200–206.
[4] P. Karaolia, I. Michael-Kordatou, E. Hapeshi, C. Drosou, Y. Bertakis, D. Christofilos, G. S. Armatas, L. Sygellou, T. Schwartz, N. P. Xekoukoulotakis, *Appl. Catal. B* **2018**, *224*, 810–824.
[5] J.-A. Quek, S.-M. Lam, J.-C. Sin, A. R. Mohamed, *J. Photochem. Photobiol. B* **2018**, *187*, 66–75.
[6] Q. Yin, L. Tan, Q. Lang, X. Ke, L. Bai, K. Guo, R. Qiao, S. Bai, *Appl. Catal. B* **2018**, *224*, 671–680.
[7] A.-Y. Zhang, W.-Y. Wang, J.-J. Chen, C. Liu, Q.-X. Li, X. Zhang, W.-W. Li, Y. Si, H.-Q. Yu, *Energy Environ. Sci.* **2018**, *11*, 1444–1448.
[8] B. Tomšič, B. Simončič, B. Orel, M. Žerjav, H. Schroers, A. Simončič, Z. Samardžija, *Carbohydr. Polym.* **2009**, *75*, 618–626.
[9] Q. Xie, Z. Xu, B. Hu, X. He, L. Zhu, *Microsc. Res. Tech.* **2017**, *80*, 272–279.
[10] M. Lanz, D. SchuÈrch, G. Calzaferri, *J. Photochem. Photobiol. A* **1999**, *120*, 105–117.
[11] V. R. Reddy, A. Currao, G. Calzaferri, *J. Mater. Chem.* **2007**, *17*, 3603–3609.
[12] H. Wang, X. Lang, J. Gao, W. Liu, D. Wu, Y. Wu, L. Guo, J. Li, *Chem. Eur. J.* **2012**, *18*, 4620–4626.
[13] L. Wang, M. Yu, C. Wu, N. Deng, C. Wang, X. Yao, *Adv. Synth. Catal.* **2016**, *358*, 2631–2641.
[14] F. Cao, Y. Wang, J. Wang, R. Deng, T. Zhou, H. Liu, B. Wu, J. Zhou, S. Li, G. Qin, *Chem. Lett.* **2017**, *47*, 92–94.
[15] S. Bao, Z. Wang, X. Gong, C. Zeng, Q. Wu, B. Tian, J. Zhang, *J. Mater. Chem. A* **2016**, *4*, 18570–18577.
[16] Z. Wang, D. Cao, L. Wen, R. Xu, M. Obergfell, Y. Mi, Z. Zhan, N. Nasori, J. Demsar, Y. Lei, *Nat. Commun.* **2016**, *7*, 10348.
[17] S. M. Kim, S. W. Lee, S. Y. Moon, J. Y. Park, *J. Phys. Condens. Matter* **2016**, *28*, 254002.
[18] P. Vasa, C. Lienau, *ACS Photonics* **2017**, *5*, 2–23.
[19] M. L. Brongersma, N. J. Halas, P. Nordlander, *Nat. Nanotechnol.* **2015**, *10*, 25.
[20] K. G. Stamplecoskie, J. C. Scaiano, *J. Am. Chem. Soc.* **2010**, *132*, 1825–1827.
[21] A. F. Wady, A. L. Machado, C. C. Foggi, C. A. Zamperini, V. Zucolotto, E. B. Moffa, C. E. Vergani, *J. Nanomater.* **2014**, *2014*, 128.
[22] L. Wei, J. Lu, H. Xu, A. Patel, Z.-S. Chen, G. Chen, *Drug Discovery Today* **2015**, *20*, 595–601.
[23] Z. Guo, G. Chen, G. Zeng, J. Liang, B. Huang, Z. Xiao, F. Yi, Z. Huang, K. He, *Environ. Sci. Nano* **2016**, *3*, 1027–1035.
[24] H. D. Beyene, A. A. Werkneh, H. K. Bezabh, T. G. Ambaye, *Sustain. Mater. Technol.* **2017**, *13*, 18–23.
[25] Z. Huang, G. Chen, G. Zeng, Z. Guo, K. He, L. Hu, J. Wu, L. Zhang, Y. Zhu, Z. Song, *J. Hazard. Mater.* **2017**, *321*, 37–46.
[26] Y. Yan, H. Xing, C. Han, A. Yang, *Ceram. Int.* **2017**, *43*, 3905–3909.
[27] M. Assis, T. Robeldo, C. C. Foggi, A. M. Kubo, G. Mínguez-Vega, E. Condoncillo, H. Beltran-Mir, R. Torres-Mendieta, J. Andrés, M. Oliva, et al., *Sci. Rep.* **2019**, *9*, 9927.
[28] S. Liu, J. Tian, L. Wang, X. Sun, *Carbon N. Y.* **2011**, *49*, 3158–3164.
[29] Q. Deng, X. Duan, D. H. L. Ng, H. Tang, Y. Yang, M. Kong, Z. Wu, W. Cai, G. Wang, *ACS Appl. Mater. Interfaces* **2012**, *4*, 6030–6037.
[30] K.-H. Chen, Y.-C. Pu, K.-D. Chang, Y.-F. Liang, C.-M. Liu, J.-W. Yeh, H.-C. Shih, Y.-J. Hsu, *J. Phys. Chem. C* **2012**, *116*, 19039–19045.
[31] L. Amirav, A. P. Alivisatos, *J. Phys. Chem. Lett.* **2010**, *1*, 1051–1054.
[32] D. B. Ingram, S. Linic, *J. Am. Chem. Soc.* **2011**, *133*, 5202–5205.
[33] S. Linic, P. Christopher, D. B. Ingram, *Nat. Mater.* **2011**, *10*, 911.
[34] P. V. Kamat, *J. Phys. Chem. Lett.* **2012**, *3*, 663–672.
[35] X. Zhang, Y. L. Chen, R.-S. Liu, D. P. Tsai, *Reports Prog. Phys.* **2013**, *76*, 46401.
[36] S. K. Cushing, A. D. Bristow, N. Wu, *Phys. Chem. Chem. Phys.* **2015**, *17*, 30013–30022.
[37] H. Hu, Z. Jiao, T. Wang, J. Ye, G. Lu, Y. Bi, *J. Mater. Chem. A* **2013**, *1*, 10612–10616.
[38] S. T. Kochuveedu, Y. H. Jang, D. H. Kim, *Chem. Soc. Rev.* **2013**, *42*, 8467–8493.
[39] W. Fan, Y. H. Lee, S. Pedireddy, Q. Zhang, T. Liu, X. Y. Ling, *Nanoscale* **2014**, *6*, 4843–4851.
[40] W. Zhao, Y. Guo, Y. Faiz, W.-T. Yuan, C. Sun, S.-M. Wang, Y.-H. Deng, Y. Zhuang, Y. Li, X.-M. Wang, et al., *Appl. Catal. B* **2015**, *163*, 288–297.
[41] Y. Choi, M. S. Koo, A. D. Bokare, D. Kim, D. W. Bahnemann, W. Choi, *Environ. Sci. Technol.* **2017**, *51*, 3973–3981.
[42] D. Liu, W. Huang, L. Li, L. Liu, X. Sun, B. Liu, B. Yang, C. Guo, *Nanotechnology* **2017**, *28*, 385702.
[43] J. Li, F. Liu, Y. Li, *New J. Chem.* **2018**, *42*, 12054–12061.
[44] C. An, S. Wang, Y. Sun, Q. Zhang, J. Zhang, C. Wang, J. Fang, *J. Mater. Chem. A* **2016**, *4*, 4336–4352.
[45] J.-Q. Xiao, N. V. Mdlovu, K.-S. Lin, C.-J. Chang, Z.-W. Chen, *Catal. Today* **2019**, DOI https://doi.org/10.1016/j.cattod.2019.10.010.
[46] Z. Yu, Y. Liu, W. He, Z. Wang, *Catal. Today* **2019**.
[47] D. K. Bhatt, U. D. Patel, *J. Phys. Chem. Solids* **2019**, *135*, 109118.
[48] P. Wang, B. Huang, X. Qin, X. Zhang, Y. Dai, J. Wei, M.-H. Whangbo, *Angew. Chem. Int. Ed.* **2008**, *47*, 7931–7933.
[49] J. Liao, K. Zhang, L. Wang, W. Wang, Y. Wang, J. Xiao, L. Yu, *Mater. Lett.* **2012**, *83*, 136–139.

ChemistrySelect

Full Papers
doi.org/10.1002/slct.202000502

Chemistry
Europe
European Chemical
Societies Publishing

[50] Y. Bi, J. Ye, *Chem. Commun.* **2009**, 6551–6553.

[51] C. An, S. Peng, Y. Sun, *Adv. Mater.* **2010**, *22*, 2570–2574.

[52] H. Xu, H. Li, J. Xia, S. Yin, Z. Luo, L. Liu, L. Xu, *ACS Appl. Mater. Interfaces* **2011**, *3*, 22–29.

[53] L. Han, Z. Xu, P. Wang, S. Dong, *Chem. Commun.* **2013**, *49*, 4953–4955.

[54] S.-F. Yang, C.-G. Niu, D.-W. Huang, H. Zhang, C. Liang, G.-M. Zeng, *Environ. Sci. Nano* **2017**, *4*, 585–595.

[55] L. Kuai, B. Geng, X. Chen, Y. Zhao, Y. Luo, *Langmuir* **2010**, *26*, 18723–18727.

[56] Z. Wang, J. Liu, W. Chen, *Dalton Trans.* **2012**, *41*, 4866–4870.

[57] T. Yan, H. Zhang, Q. Luo, Y. Ma, H. Lin, J. You, *Chem. Eng. J.* **2013**, *232*, 564–572.

[58] K. Naoi, Y. Ohko, T. Tatsuma, *Chem. Commun.* **2005**, 1288–1290.

[59] L. Liu, T. D. Dao, R. Kodiyath, Q. Kang, H. Abe, T. Nagao, J. Ye, *Adv. Funct. Mater.* **2014**, *24*, 7754–7762.

[60] C. An, R. Wang, S. Wang, X. Zhang, *J. Mater. Chem.* **2011**, *21*, 11532–11536.

[61] Z. Lou, B. Huang, P. Wang, Z. Wang, X. Qin, X. Zhang, H. Cheng, Z. Zheng, Y. Dai, *Dalton Trans.* **2011**, *40*, 4104–4110.

[62] M. Zhu, P. Chen, M. Liu, *J. Mater. Chem.* **2011**, *21*, 16413–16419.

[63] D. Chen, S. H. Yoo, Q. Huang, G. Ali, S. O. Cho, *Chem.- A Eur. J.* **2012**, *18*, 5192–5200.

[64] S. Mao, R. Bao, D. Fang, J. Yi, *Adv. Powder Technol.* **2018**, *29*, 2670–2677.

[65] J. Gong, H. Liu, Y. Jiang, S. Yang, X. Liao, Z. Liu, S. Ringer, *Mater. Charact.* **2015**, *110*, 1–4.

[66] A. Mansourian, S. A. Paknejad, A. V. Zayats, S. H. Mannan, *J. Phys. Chem. C* **2016**, *120*, 20310–20314.

[67] C. Ma, X. Chen, X. Tan, P. Hu, Q. Li, Y. Cao, X. Liang, *CrystEngComm* **2018**, *20*, 2227–2232.

[68] E. Longo, L. S. Cavalcante, D. P. Volanti, A. F. Gouveia, V. M. Longo, J. A. Varela, M. O. Orlandi, J. Andrés, *Sci. Rep.* **2013**, *3*, 1676.

[69] E. Longo, D. P. Volanti, V. M. Longo, L. Gracia, I. C. Nogueira, M. A. P. Almeida, A. N. Pinheiro, M. M. Ferrer, L. S. Cavalcante, J. Andrés, *J. Phys. Chem. C* **2014**, *118*, 1229–1239.

[70] M. T. Fabbro, C. Saliby, L. R. Rios, F. A. La Porta, L. Gracia, M. S. Li, J. Andrés, L. P. S. Santos, E. Longo, *Sci. Technol. Adv. Mater.* **2015**, *16*, 65002.

[71] R. A. Roca, A. F. Gouveia, P. S. Lemos, L. Gracia, J. Andrés, E. Longo, *Inorg. Chem.* **2016**, *55*, 8661–8671.

[72] J. Andrés, A. F. Gouveia, L. Gracia, E. Longo, G. Manzeppi Faccin, E. Z. da Silva, D. H. Pereira, M. A. San-Miguel, *Int. J. Quantum Chem.* **2018**, *118*, e25551.

[73] N. G. Macedo, T. R. Machado, R. A. Roca, M. Assis, C. C. Foggi, V. Puerto-Belda, G. Mínguez-Vega, A. Rodrigues, M. A. San-Miguel, E. Cordoncillo, *ACS Appl. Bio Mater.* **2019**, *2*, 824–837.

[74] L. P. S., S. G. S., R. R. A., A. M. T.-M. R. B.-M. H., M.-V. G., C. E., A. J., L. E., *Phys. Chem. Chem. Phys.* **2019**, *21*, 6101–6111.

[75] E. V. Formo, W. Fu, A. J. Rondinone, S. Dai, *RSC Adv.* **2012**, *2*, 9359–9361.

[76] G. Shi, S. Bao, W. Lai, Z. Rao, X. Zhang, Z. Wang, *Scanning* **2013**, *35*, 69–74.

[77] P. V. Asharani, Y. l. Lianwu, Z. Gong, S. Valiyaveettil, *Nanotoxicology* **2011**, *5*, 43–54.

[78] P. F. S. Pereira, A. F. Gouveia, M. Assis, R. C. de Oliveira, I. M. Pinatti, M. Penha, R. F. Gonçalves, L. Gracia, J. Andrés, E. Longo, *Phys. Chem. Chem. Phys.* **2018**, *20*, 1923–1937.

[79] A. B. Trench, T. R. Machado, A. F. Gouveia, M. Assis, L. G. da Trindade, C. Santos, A. Perrin, C. Perrin, M. Oliva, J. Andrés, et al., *Appl. Catal. B* **2018**, *238*, 198–211.

[80] N. G. Macedo, A. F. Gouveia, R. A. Roca, M. Assis, L. Gracia, J. Andrés, E. R. Leite, E. Longo, *J. Phys. Chem. C* **2018**, *122*, 8667–8679.

[81] B. Cai, J. Wang, S. Gan, D. Han, Z. Wu, L. Niu, *J. Mater. Chem. A* **2014**, *2*, 5280–5286.

[82] X.-J. Wen, C.-H. Shen, Z.-H. Fei, D. Fang, Z.-T. Liu, J.-T. Dai, C.-G. Niu, *Chem. Eng. J.* **2019**, 123083.

[83] E. A. Pillar, M. I. Guzman, J. M. Rodriguez, *Environ. Sci. Technol.* **2013**, *47*, 10971–10979.

[84] J. Zhang, Y. Zhang, X. Ren, G. Cui, A. M. Asiri, B. Zheng, X. Sun, *Eng* **2017**, *5*, 8908–8917.

[85] M. Westerfield, *http//zfin. org/zf_nfo/zfbook/zfbk. html* **2000**

[86] Oecd, *OECD Guidelines for the Testing of Chemicals*, Organization For Economic, **1994**

[87] C. B. Kimmel, W. W. Ballard, S. R. Kimmel, B. Ullmann, T. F. Schilling, *Dev. Dyn.* **1995**, *203*, 253–310.

[88] G. Kresse, J. Furthmüller, *Comput. Mater. Sci.* **1996**, *6*, 15–50.

[89] J. P. Perdew, K. Burke, M. Ernzerhof, *Phys. Rev. Lett.* **1996**, *77*, 3865–3868.

[90] S. Hull, D. A. Keen, *Phys. Rev. B* **1999**, *59*, 750–761.

[91] R. C. Hanson, T. A. Fjeldly, H. D. Hochheimer, *Phys. Status Solidi* **1975**, *70*, 567–576.

[92] G. Burley, *J. Chem. Phys.* **1963**, *38*, 2807–2812.

[93] H. J. Fan, L. D. Marks, *Ultramicroscopy* **1989**, *31*, 357–364.

[94] K. Young-Min, K. Yang-Soo, K. Youn-Joong, *Microsc. Microanal.* **2007**, *13*, 1294–1295.

[95] S. W. Han, Y. Park, Y. H. Hwang, S. Jekal, M. Kang, W. G. Lee, W. Yang, G.-D. Lee, S. C. Hong, *Sci. Rep.* **2016**, *6*, 38730.

[96] L. Yao, S. Majumdar, L. Äkäslompolo, S. Inkinen, Q. H. Qin, S. van Dijken, *Eur. Microsc. Congr. 2016 Proc.* **2016**, 1020–1021.

[97] I. L. Validžić, V. Jokanović, D. P. Uskoković, J. M. Nedeljković, *J. Eur. Ceram. Soc.* **2007**, *27*, 927–929.

[98] I. Martina, R. Wiesinger, D. Jembrih-Simbürger, M. Schreiner, *E-Preserv Sci* **2012**, *9*, 1–8.

[99] G. L. Bottger, C. V. Damsgard, *Solid State Commun.* **1971**, *9*, 1277–1280.

[100] G. L. Bottger, C. V. Damsgard, *J. Chem. Phys.* **1972**, *57*, 1215–1218.

[101] P. Kubelka, *Zeitschrift fur Tech. Phys.* **1931**, *12*, 593–601.

[102] D. L. Wood, J. Tauc, *Phys. Rev. B* **1972**, *5*, 3144–3151.

[103] A. B. Gordienko, Y. N. Zhuravlev, A. S. Poplavnoi, *Phys. Status Solidi* **1991**, *168*, 149–156.

[104] A. Dashora, A. Marwal, K. R. Soni, B. L. Ahuja, *Pramana* **2010**, *74*, 1017–1027.

[105] F. Urbach, *Phys. Rev.* **1953**, *92*, 1324.

[106] V. M. Longo, L. S. Cavalcante, A. T. de Figueiredo, L. P. S. Santos, E. Longo, J. A. Varela, J. R. Sambrano, C. A. Paskocimas, F. S. De Vicente, A. C. Hernandes, *Appl. Phys. Lett.* **2007**, *90*, 91906.

[107] J. Milanez, A. T. de Figueiredo, S. de Lazaro, V. M. Longo, R. Erlo, V. R. Mastelaro, R. W. A. Franco, E. Longo, J. A. Varela, *J. Appl. Phys.* **2009**, *106*, 43526.

[108] L. Gracia, V. M. Longo, L. S. Cavalcante, A. Beltrán, W. Avansi, M. S. Li, V. R. Mastelaro, J. A. Varela, E. Longo, J. Andrés, *J. Appl. Phys.* **2011**, *110*, 43501.

[109] G. S. Silva, L. Gracia, M. T. Fabbro, L. P. Serejo dos Santos, H. Beltrán-Mir, E. Cordoncillo, E. Longo, J. Andrés, *Inorg. Chem.* **2016**, *55*, 8961–8970.

[110] R. C. de Oliveira, C. C. de Foggi, M. M. Teixeira, M. D. P. da Silva, M. Assis, E. M. Francisco, B. N. A. da S. Pimentel, P. F. dos S. Pereira, C. E. Vergani, A. L. Machado, et al., *ACS Appl. Mater. Interfaces* **2017**, *9*, 11472–11481.

[111] J. R. G. Patnaik, C. S. Sunandana, *J. Phys. Chem. Solids* **1998**, *59*, 1059–1069.

[112] X. Zhao, Y. Zhu, *Environ. Sci. Technol.* **2006**, *40*, 3367–3372.

[113] X. Cheng, Q. Cheng, X. Deng, P. Wang, H. Liu, *Electrochim. Acta* **2015**, *184*, 264–275.

[114] G. Botelho, J. Andres, L. Gracia, L. S. Matos, E. Longo, *ChemPlusChem* **2016**, *81*, 202–212.

[115] M. Rehan, T. A. Khattab, A. Barohum, L. Gätjen, R. Wilken, *Carbohydr. Polym.* **2018**, *197*, 227–236.

[116] Q. Ma, H. Zhang, R. Guo, Y. Cui, X. Deng, X. Cheng, M. Xie, Q. Cheng, B. Li, *J. Inst. Chem.* **2017**, *80*, 176–183.

[117] R. Dong, B. Tian, C. Zeng, T. Li, T. Wang, J. Zhang, *J. Phys. Chem. C* **2013**, *117*, 213–220.

[118] V. M. Longo, C. C. De Foggi, M. M. Ferrer, A. F. Gouveia, R. S. André, W. Avansi, C. E. Vergani, A. L. Machado, J. Andrés, L. S. Cavalcante, et al., *J. Phys. Chem. A* **2014**, *118*, 5769–5778.

[119] P. Zhou, J. Yu, M. Jaroniec, *Adv. Mater.* **2014**, *26*, 4920–4935.

[120] Z. Zheng, C. Chen, A. Bo, F. S. Zavahir, E. R. Waclawik, J. Zhao, D. Yang, H. Zhu, *ChemCatChem* **2014**, *6*, 1210–1214.

[121] C. Liang, H. Guo, L. Zhang, L. Ruan, C.-G. Niu, H.-P. Feng, X.-J. Wen, N. Tang, H.-Y. Liu, G.-M. Zeng, *Chem. Eng. J.* **2019**, *372*, 12–25.

[122] R. Memming, in (Ed.: E. Steckhan), Springer Berlin Heidelberg, Berlin, Heidelberg, **1988**, pp. 79–112.

[123] C. H. Gammons, Y. Yu, *Chem. Geol.* **1997**, *137*, 155–173.

[124] C. Krishnaraj, S. L. Harper, S.-I. Yun, *J. Hazard. Mater.* **2016**, *301*, 480–491.

[125] S. Nangia, R. Sureshkumar, *Langmuir* **2012**, *28*, 17666–17671.

[126] C. R. Walters, E. J. Pool, V. S. Somerset, *J. Environ. Sci. Health Part A* **2014**, *49*, 1588–1601.

[127] B. D. Williams, J. A. Denhom, *J. Weather Modif.* **2009**, *41*, 75–96.

[128] C. Fajardo, G. Costa, L. T. Ortiz, M. Nande, M. L. Rodríguez-Membibre, M. Martín, S. Sánchez-Fortún, *Ecotoxicol. Environ. Saf.* **2016**, *133*, 433–441.

[129] K. J. Lee, L. M. Browning, P. D. Nallathamby, C. J. Osgood, X.-H. N. Xu, *Nanoscale* **2013**, *5*, 11625–11636.

[130] K. J. Groh, T. Dalkvist, F. Piccapietra, R. Behra, M. J.-F. Suter, K. Schirmer, *Nanotoxicology* **2015**, *9*, 81–91.

[131] A. M. Iniyan, R. R. Kannan, F.-J. R. S. Joseph, T. R. J. Mary, M. Rajasekar, P. C. Sumy, A. M. Rabel, D. Ramachandran, S. G. P. Vincent, *Microb. Pathog.* **2017**, *112*, 76–82.

[132] J. R. F. Elphick, K. D. Bergh, H. C. Bailey, *Environ. Toxicol. Chem.* **2011**, *30*, 239–246.

[133] G. De Boeck, A. Vlaeminck, A. Van der Linden, R. Blust, *Physiol. Biochem. Zool.* **2000**, *73*, 102–111.

[134] C. F. Cooper, W. C. Jolly, *Water Resour. Res.* **1970**, *6*, 88–98.

[135] H. T. Ratte, *Environ. Toxicol. Chem.* **1999**, *18*, 89–108.